Journal of Wind Engineering & Industrial Aerodynamics 242 (2023) 105574

Contents lists available at ScienceDirect

Journal of Wind Engineering & Industrial Aerodynamics

journal homepage: www.elsevier.com/locate/jweia

Sparse-measurement-based peak wind pressure evaluation by super-resolution convolutional neural networks

Haokai Wu [b], Yaoran Chen [c], Peixing Xie [b], Dai Zhou [a,b], Tetsuro Tamura [d], Kai Zhang [a,b], Shuyang Cao [e], Yong Cao [a,b,f,*]

[a] State Key Laboratory of Ocean Engineering, Shanghai Key Laboratory for Digital Maintenance of Buildings and Infrastructure, Shanghai Jiao Tong University, Shanghai, 200240, China
[b] School of Naval Architecture, Ocean and Civil Engineering, Shanghai Jiao Tong University, Shanghai, 200240, China
[c] School of Artificial Intelligence Institute, Shanghai University, Shanghai, 200444, China
[d] Department of Architecture and Building Engineering, Tokyo Institute of Technology, Yokohama, 226-8502, Japan
[e] College of Civil Engineering, Tongji University, Shanghai, 200092, China
[f] Chongqing Research Institute, Shanghai Jiao Tong University, Chongqing, 401135, China

ARTICLE INFO

Keywords:
Peak wind pressure
Building facades
Convolutional neural networks
Super-resolution reconstruction
Time-filtered

ABSTRACT

An accurate estimation of the extreme wind pressure acting on glazed panels is essential for the wind-resistant design of buildings. The traditional time-length-velocity (TVL) approach is severely dependent on the determination of the TVL factors and the selection of single-point measurement tap. To overcome the difficulties, this study aims to generate a generalized model based on convolutional neural network (CNN) to reconstruct the super-resolution pressure distributions from low-resolution pressure measurements at different wind directions. The constraint represented by the pressure gradient are embedded in the loss function of the CNN to enable the model to generate real pressure distribution characteristics. By spatially averaging the super-resolution distributions, the peak space-averaged pressure on the glazed panels could be finally predicted. On the basis of a rectangle-section high-rise building, the regions near the top corner and near the middle-height under different wind directions are focused on. Results show that the pressure peaks computed from the super-resolution distributions can provide more accurate and robust representations for the true area-averaged peaks, compared with the traditional TVL method. The generalization ability of the pressure gradient guided SRCNN is systematically investigated among different pressure modes and flow patterns influenced by the incident angles.

1. Introduction

In design of the lightweight buildings, glazed panels are widely utilized in the exterior cladding layer, which are often destroyed by local extreme wind loadings. From the point of wind resistance and disaster mitigation, it is indispensable to accurately evaluate the extreme design wind pressure on glazed panels. In principle, the extreme design wind pressures are estimated on the basis of the area-averaged loading over a panel, which can be directly integrated from the pressure distributions over the panel in the ideal situation. However, the accuracy of area averaging is strongly dependent on the density of the setup of pressure measurement taps. Due to the economic and technical limitations, sparse measurements (less than 10 pressure taps within a 10 m^2 full-scale surface in average) were often installed in the previous field observations or wind-tunnel experiments, which resulted in the rough pressure estimations (Huang et al., 2014; Kopp et al., 2010; Zhang and Li, 2018). More recently, the high-resolution pressure measurements (more than 80 taps within a 10 m^2 full-scale surface in average) were carried out in the atmospheric boundary layer (ABL) wind tunnel of the Politecnico di Milano (PoliMi). The time series of pressure was recorded at each measurement tap to build up a pressure database of high-rise building facades (Lamberti et al., 2020; Pomaranzi et al., 2022). But so far, high-precision experimental data have still been scarce due to its high cost and technical difficulties. Thus, it remains a big question how to improve the accuracy of evaluating peak pressures while the pressure-tap setup is sparse.

* Corresponding author. State Key Laboratory of Ocean Engineering, Shanghai Key Laboratory for Digital Maintenance of Buildings and Infrastructure, Shanghai Jiao Tong University, Shanghai, 200240, China.
E-mail address: yongcao@sjtu.edu.cn (Y. Cao).

https://doi.org/10.1016/j.jweia.2023.105574
Received 7 July 2023; Received in revised form 12 September 2023; Accepted 20 September 2023

Nearly fifty years ago, the time-length-velocity (TVL) method was proposed to approximate the peak pressures under the condition of sparse measuring taps. Inspired by the wind loading measurements performed by Newberry et al. (1973) on Royex House, Lawson (1976) first proposed the TVL equation in order to approximate the real area-averaged pressure from the pressure time-series measured at a single measurement station. The equation explained the relationship between the time-averaged window τ and the ratio of the reference length L of an area to the reference velocity V, which adopted the assumption that the duration of the peak pressure events is proportional to their spatial extent:

$$\tau = \frac{K \cdot L}{V}, \tag{1}$$

where K denotes the exponential decay factor in the spatial coherence function of the pressure signal. Once K is determined, the area-averaged pressure over a region with reference length L could be approximately represented by the time-moving averaged pressure at a single pressure tap with a moving span of τ. K was suggested to be 4.5 according to the measurements on the windward face of the Royex House. Holmes (1997) reexamined the original TVL equation and pointed out that the spatial correlation of pressures between two points could be represented more properly by the aerodynamic admittance function. He translated the admittance function into moving average filter, and suggested a modification of TVL equation to $\tau = 1.0\ L/V$. The TVL method has the advantage of simplicity in the formula that makes the method popular. Nevertheless, the ideal assumption that accounts for the area averaging by the time filtering is not easily satisfied when the pressure distributions on the building surfaces is only deduced by a simple and fixed K factor. That is because the pressures on buildings are very complex (sometimes random) in time and space, which are strongly influenced by the massive flow separation and vortex formation around the buildings. Li et al. (2021) evaluated the applicability of TVL method when predicting the pressure distribution on the roof of a 40-m-tall building. The optimal K value was found highly dependent on the selection of single-point measurement tap. Pomaranzi et al. (2022) observed that the time-filtered pressure fluctuated violently among different measurement taps although K was fixed, leading to uncertain estimations and large errors. It seems that a new concept (or method) is necessary to solve the problems evaluating peak pressures on the cladding panel in case of sparse measurement taps.

In recent decades, machine learning (ML) or deep learning methods was emerging as an ideal alternative tool to tackle the complex wind-induced problems on structure engineering. A suitable and well-trained learning model could accurately and efficiently predict the wind loadings and pressure distributions only from the limited information. Uematsu and Tsuruishi (2008) estimated the pressure coefficients at an arbitrary point on roof cladding through an artificial neural network (ANN) from the information on the dome geometry and the turbulence intensity of approaching flow. Based on the data in the wind tunnel tests, Huang et al. (2017) established a model combined orthogonal decomposition algorithm (POD) and back propagation (BP) neural network algorithm to predict mean, root-mean-square (RMS) pressure coefficients and the time series of wind-induced pressures. Li et al. (2018) applied the wind speeds and wind directions as exogenous inputs. They classified the VIV modes and modeled their responses in time domain using the decision tree learning algorithm and support vector regression. Sang et al. (2021) trained an artificial neural network (ANN) to evaluate the drag coefficients of a rectangular cross-section building, assisted by a big training dataset extracted from the large eddy simulations. Meanwhile, a series of recent studies have also made impressive contributions to shows the application potential of ML in estimation of load and vibration effects on rectangular buildings. The ML techniques, including generative adversarial network (GAN), gradient boosting regression tree (GBRT) and light gradient boosting machine (LGBM), were proved to be efficient and effective tools to predict pressure coefficients, crosswind vibrations and force spectra respectively (Hu et al., 2020; Lin et al., 2021, 2022).

Convolutional neural networks (CNN), as a representative of deep learning algorithms in machine learning, has a good performance of capturing the nonlinear spatial distribution features of measurements (Cheng et al., 2018). Super-resolution Convolutional neural network (SRCNN) is a special form of CNN, which has the function of upscaling the resolution for the data points. The spatial super-resolution practices through SRCNN have made preliminary progress in many fields, such as the satellite image reconstruction (Darren et al., 2018), turbulent flow downscaling (Fukami et al., 2020; Jin et al., 2018), wind field prediction (Chen et al., 2021) and local precipitation forecast (Rodrigues et al., 2018). To the best of the authors' knowledge, there have not been such applications of CNN-based model for the pressure reconstruction on the building facades in previous studies. Super-resolution Convolutional Neural Networks (SRCNN) is expected to be a promising tool of reproducing high-resolution pressure field from given low-resolution measurements. Direct integration of reconstructed high-resolution pressure distributions would further reflect the local pressure features and make the accurate estimation of peak area-averaged pressure on cladding panels possible. The uncertainty arisen from the TVL approach might be overcome once this new high-accuracy method is put into the application.

To summarize, novel methods are required to replace the traditional TVL method, which has the obvious limitation of estimating the area-averaged loading on cladding panels while the pressure taps are sparsely setup. To this end, the present study aims to systematically investigate the applicability of SRCNN to evaluate the peak pressure on cladding panels of a high-rise building. Fig. 1 summarizes the workflow to execute such peak pressure evaluation. Using SRCNN model, we respectively reconstruct the super-resolution pressure fields from sparse measurements at different time-steps. Based on reconstructed fields, area-averaging method is applied to predict the pressures over the panel. The predicted area-averaged pressure peaks are compared with the true ones calculated from the high-resolution experimental measurements, to assess the prediction accuracy of current SRCNN-based method. Furthermore, the effect of various pressure modes and flow patterns on the performance of pressure reconstruction and estimation of SRCNN is also analyzed by altering the wind directions acting on the building facade. Section 2 introduces the wind-tunnel experimental database of PoliMi which is used to train and validate the SRCNN model. The basic structure of the applied SRCNN and its training methodology are explained in Section 3. In Section 4, the parametric study and verification of SRCNN model can be achieved by directly comparing the super-resolution reconstructed field and the high-resolution experimental measurements, followed by peak area-averaged pressure estimation based on the SRCNN model. In Section 5, the conclusions are presented.

2. Dataset

The super-resolution pressure fields are expected by the SRCNN model. The model training and the validation of prediction accuracy require the high-resolution pressure measurements. This study utilizes the pressure database which are measured on the surfaces of a building model in the ABL wind tunnel of the PoliMi (Pomaranzi et al., 2020). The database recorded the spatial and temporal pressure variations in the most critical regions on the building facade, i.e., adjacent to the corners (Tile A) and near the edge at the middle height of the building (Tile B), as shown in Fig. 2(a). Different inflow directions (α) are also considered, including $+10°$, $-15°$, $-170°$ and $-150°$ for Tile A and $180°$, $-15°$, $-170°$ and $-135°$ for Tile B. The building model has a rectangular cross-section with dimensions of $L \times D = 1\ \text{m} \times 0.3\ \text{m}$ and a height $H = 2$ m, as indicated in Fig. 2(a). The scale ratio of the building model is 1:50, corresponding to a 100-m-tall building in full size. The blockage ratio of the model is below 3% in this tunnel. As shown in Fig. 2

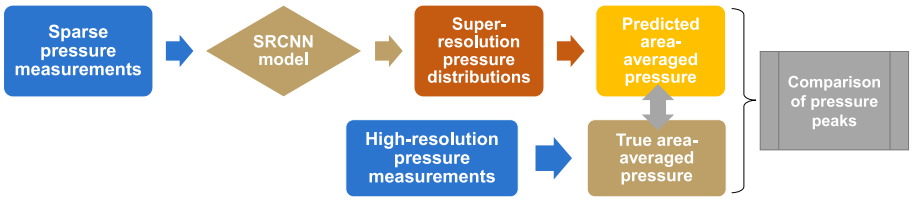

Fig. 1. Schematic overview of SRCNN-based evaluation of peak pressure over the cladding panel.

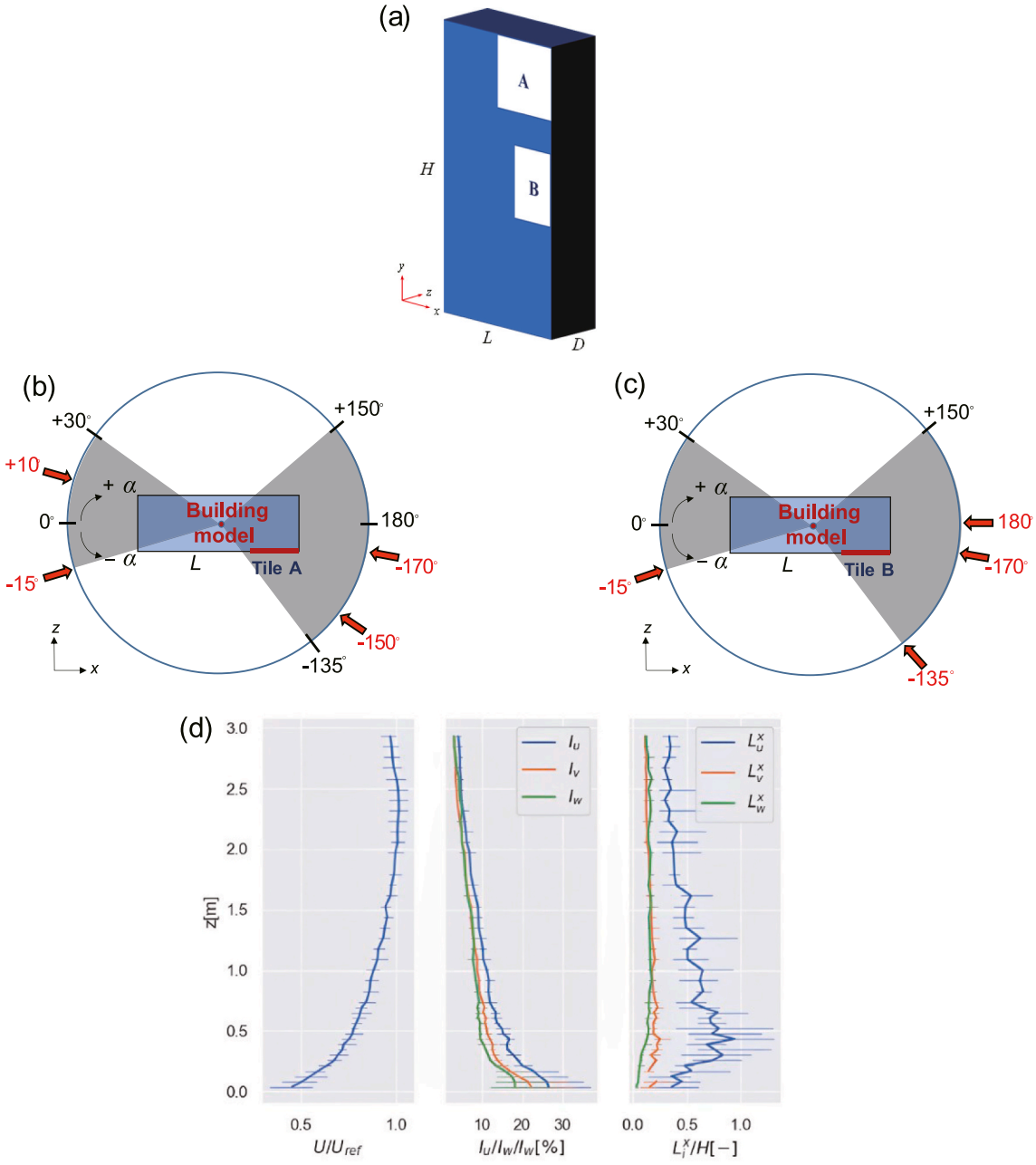

Fig. 2. (a) Three-dimensional view of the building model. (b) Wind directions investigated for Tile A. (c) Wind directions investigated for Tile B from the top view. The present investigated wind directions are indicated in red. The grey zones are wind direction ranges investigated for both tiles in PoliMi. (d) Wind profiles applied in the PoliMi tests with error bars representing spanwise variation. Left: mean speed profile. Center: Turbulence intensity. Right: Integral length scales (Lamberti et al., 2020).

(b) and (c), the present work focuses on the construction of pressure distributions and the prediction of extreme pressure values on Tile A and Tile B at five wind directions indicated by red arrows, including windward and leeward cases. Both tiles tend to experience some representative pressure fluctuation modes as the wind direction rotates. Fig. 2(d) presents the wind profiles employed for the PoliMi test, including mean speed profile (Left), turbulence intensity (Center) and integral length scales (right), averaged over the five cross-flow locations (Lamberti et al., 2020).

As a merit of the database, pressure taps were densely arranged on Tile A and Tile B, where approximately 200 pressure taps are set respectively on each tile. The distance between two taps is very short in comparison with most of previous wind-tunnel experiments, with the minimum distance reaching 3 mm (corresponding to 0.15 m in full scale) near the building edges. The distance increases progressively when moving away from the edges in Fig. 3(a) and (b). The wind speed was 11.7 m/s and the streamwise turbulence intensity was approximately 0.07 at the building height of 2 m in the experiments. The velocity scale ratio of boundary layer modeling was 1:2.35, implying a full-scale design wind speed of 27.5 m/s. The wind-tunnel database consisted of time series at each pressure tap, with a total duration of 300 s. The total duration corresponds to 3500 convective times normalized by the wind speed at building height (v_{ref}) and the 1m building width (d). The "convective times" represents characteristic period number that the wind field passes through the building model. High convective times ensure that we can obtain sufficient statistical information of the wind field and the pressure load around the building facade. At each wind direction, 150000 pressure snapshots were collected.

3. Super-resolution convolutional neural network model

This section shall introduce the super-resolution convolutional neural network (SRCNN), which establishes the mapping between low- and super-resolution pressure snapshots. The detailed illustrations of data-processing and SRCNN model are presented in Subsections 3.1 and Subsection 3.2, respectively.

3.1. Pre-processing of pressure database

To generate a universal SRCNN model that could be applicable to the peak pressure predictions at a given wind direction, data from four wind directions, i.e., $\alpha = +30°$, $-10°$, $-160°$ and $+160°$, are selected as training and validation sets, as indicated by red arrows in Fig. 4(a) and (b). These incident directions will lead to different flow patterns around the facade regions we considered, including the impinging flow, shear layer separation and reattachment, formation of inverted conical vortex and so on. They are expected to help the model learn more spatial variation characteristics of pressure influenced by the wind incident angles based on as few training data as possible. For each wind direction selected, the wind pressure data of 60000 time-steps in the front sequence are selected to generate the training set, 80% of which are extracted randomly only using for training while the remaining 20% are used for validation. From each given wind direction to be predicted, as exhibited by blue fonts in Fig. 4, the last 90000 time-steps data are utilized as the testing set. The testing wind directions are ensured not to be included in the four directions used in training and validation sets. Such training and validation datasets totally comprise 2550s full-scale data, while 3825 s data and more than 2000 convective times are included in testing set. The above split plan ensures that the statistical analysis of extreme wind pressure values predicted by the SRCNN model could be carried out within a sufficient testing period.

For the pre-processing, original resolution data of 224 taps on Tile A and 166 taps on Tile B nearest the building edges in the wind tunnel test were applied as main part of the output labels of the SRCNN model, which are represented by red asterisks within the model scale domain in Fig. 5(a) and (b). Considering the feasibility of convolution operations in model training stage, two-dimensional spline interpolation method was employed to complement the missing pressure measurements denoted by the green dots in Fig. 5(a) and (b), forming the final target outputs with the dimensions of 15×15 and 15×12 for Tile A and B respectively. The above interpolation method manages to generate the interpolation results with good space smoothness. Low-resolution pressure matrices were fed as input data to the model. The data at the tap farthest from the side wall in each 3×3 high-resolution point patch was extracted to constitute a relatively sparse matrix, as shown in the blue dots in Fig. 5(a) and (b). The dimensions of the sparse input data on Tile A and B are 5×5 and 5×4, respectively.

For exploring the influence of the amount of training data, namely, the sampling frequency of training samples, on the pressure reconstruction ability of the model, 1000, 6000, 10000 and 60000 sample pairs from each wind direction were chosen in the training set at the intervals of 60, 10, 6 and 1 time-steps respectively to generate four training subsets for comparative tests. We are intended to train a universal SRCNN model for pressure reconstruction and prediction at various wind directions.

3.2. SRCNN neural networks

SRCNN model is trained to predict the 5×5 low-resolution pressure matrices to 15×15 super-resolution matrices. The 3×3 times finer super-resolution model is denoted as $3 \times$ SRCNN hereafter. The architecture of $3 \times$ SRCNN model is shown in Fig. 6, which retains the basic module called "Generator" that is simplified from the super-resolution generative adversarial network (SRGAN) proposed by Wang et al. (2019). The original GAN model is composed of two modules: generator and discriminator. The generator is used to generate the spatial data distribution that approaches to the truth, and the discriminator aims to distinguish the generated data from the true ones as possible. In the process of training iterations, the accuracy of data generation was improved by a dynamic game mechanism between two modules. The SRGAN is developed from the original GAN model. Its framework was specifically introduced for the reconstruction of high-resolution turbulent flow field with the high dimensions (beyond 100 along each direction) in recent years. The commendable reconstruction accuracy was

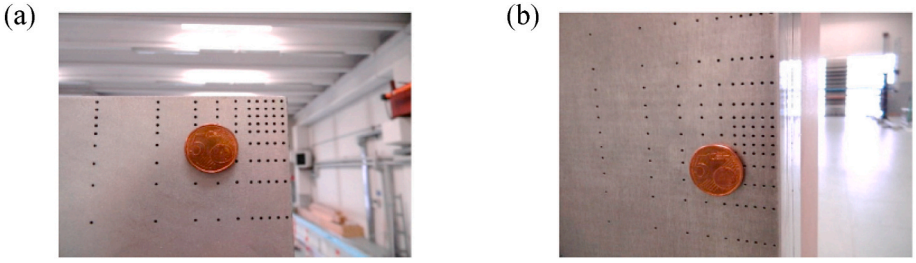

Fig. 3. Pressure tap distributions on (a) Tile A and (b) Tile B on the building model at PoliMi (Lamberti et al., 2020) A five-euro coin with diameter of 24.25 mm is taken as a reference object for the density of the pressure taps in each tile.

Fig. 4. Wind directions used in training (indicated by red arrows) and testing set (indicated by blue fonts) of SRCNN model for (a) Tile A and (b) Tile B. The wind direction range concerned in PoliMi test is represented by the grey zone.

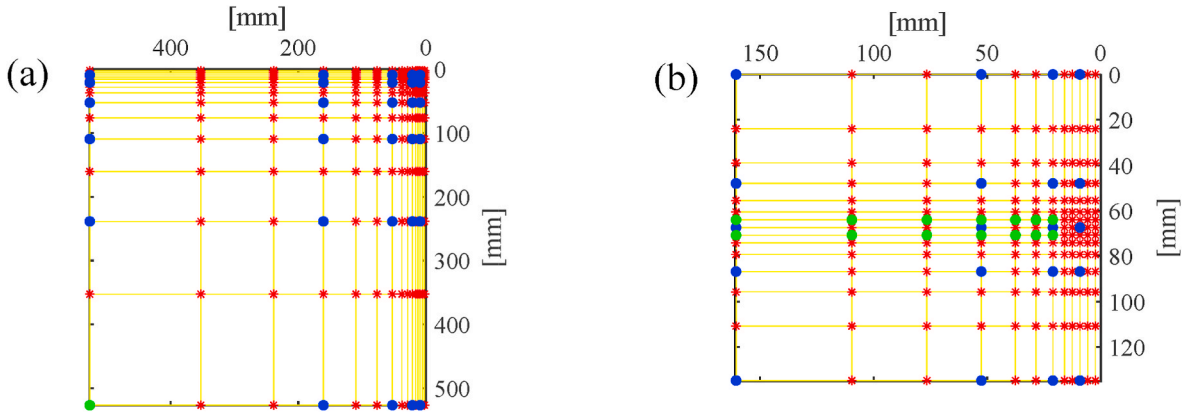

Fig. 5. High and low-resolution distributions of pressure taps on (a) Tile A and (b) Tile B. Low-resolution input taps to the SRCNN model consist of the blue dots. High-resolution output taps are comprised of the original measurements denoted by red asterisks and the interpolated ones indicated by the green dots.

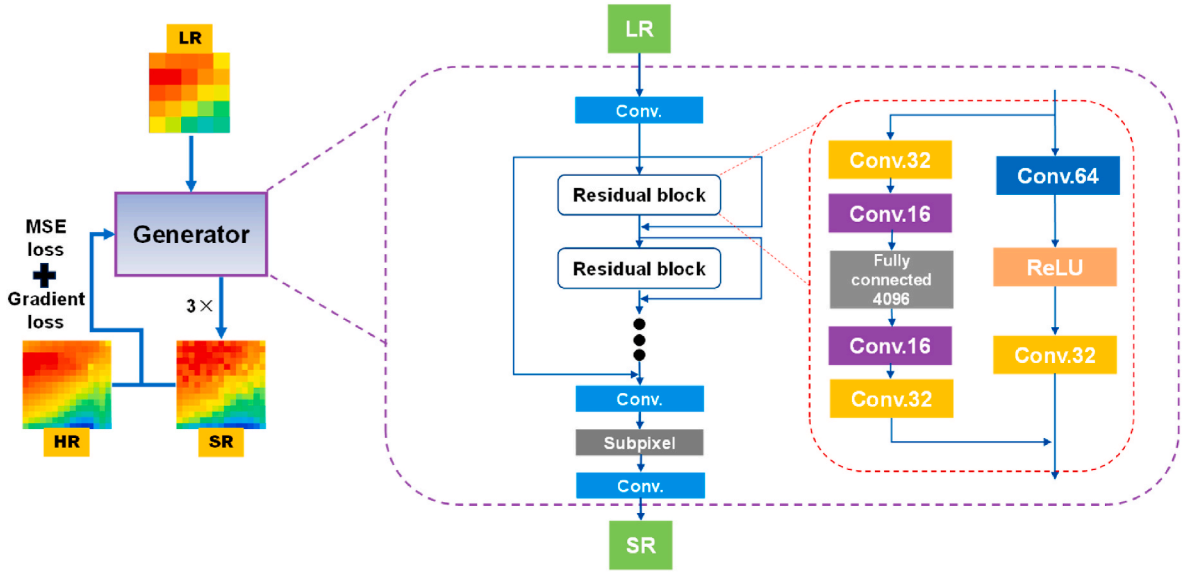

Fig. 6. SRCNN architecture. The "Generator" is applied to generate super-resolution (SR) pressure distributions from the low-resolution inputs (LR) of pressure measurements. The loss function (MSE loss plus pressure gradient loss) is calculated between the true high-resolution (HR) and SR fields. 16 layers of "Residual layers" formulate the main feature extraction framework of "Generator". A "Residual block" layer includes a parallel encoder structure.

achieved for the tiny spatial details through the SRGAN model (Stengel et al., 2020; Yousif et al., 2021, 2022). Considering the high complexity of GAN architecture, the research does not directly apply the GAN to the super-resolution processing of pressure data with the current dimensions but only keeps its convolutional generator module to save training time and computing resource. The generator is built up with a deep fully convolutional architecture, containing 16 successive residual blocks with skip connections (He et al., 2016) as presented in Fig. 6. The successive residual block structure contributes to relieving the problem of vanishing gradient descent during the training stage. A parallel encoder

structure is included in each residual block. It contains two branches, each of which contains several convolutional layers. The numbers marked in the convolutional modules represent how many feature channels the convolutional layers extract. Thus, these two branches are used to extract different levels of features from the input by using different number of filter channels, which is beneficial to make the details of the generated field closer to the truth (Jin et al., 2018). In each residual block, the rectified linear unit (ReLU) is applied as activation function. It is defined as $f(x) = \max(0, x)$, meaning that the output is the maximum value between 0 and the input x.

After introducing the whole architecture, the basic running process of the "Generator" is broken down step by step.

Step 1 The low-resolution pressure input is divided into smaller overlapping patches by the first convolutional layer.

Step 2 The SRCNN's residual layers are responsible for extracting features from the input patch. Each residual block uses a sequence of convolutional kernel filters with different sizes to convolve over the patches, capturing various spatial variation patterns of the pressure field in various scales. Crucially, the ReLU layer embedded in each residual block introduces non-linearities and helps to learn complex relationships between low-resolution and high-resolution filed patches.

Step 3 The non-linearly features extracted from the residual layers are passed through another layer, known as the deconvolutional layer. It uses another set of filters to convolve over the features and reconstruct the super-resolution patches. The patches are overlapped to form the final super-resolution filed.

Step 4 A loss function is employed to measure the difference between super- and high-resolution filed. To minimize the loss function, the process comes back to Step 1–3 to update the parameters in each layer of the model iteratively, which is known as back-propagation. As the loss function declines fully, the "Generator" would successfully reconstruct a field approaching to the truth and the running process could be stopped.

The above training process is conducted on tensorflow-1.14.0-CPU environment. The training and validation loss function is defined as a combination of two different loss terms:

$$L(x, y) = L_{MSE} + \beta \cdot L_{gradient}, \tag{2}$$

where

$$L_{MSE} = \|y - G(x)\|_2^2, \tag{3}$$

represents a pixel-based mean-squared error (MSE), where y denotes the true high-resolution pressure field (referring to HR), x is the low-resolution input (LR), and $G(x)$ denotes the super-resolution output generated from x by SRCNN model (SR). The relationship among HR, LR and SR is also shown in Fig. 6. $L_{gradient}$ is the error calculated from the pressure gradients, which can be defined by:

$$L_{gradient} = \left| \left(\frac{\partial p}{\partial x}\right)_{\mathrm{HR}} - \left(\frac{\partial p}{\partial x}\right)_{\mathrm{SR}} \right| + \left| \left(\frac{\partial p}{\partial y}\right)_{\mathrm{HR}} - \left(\frac{\partial p}{\partial y}\right)_{\mathrm{SR}} \right| \tag{4}$$

where $\partial p/\partial x$ and $\partial p/\partial y$ are discretized with a first-order linear upwind scheme in horizontal and vertical directions respectively. The subscripts "HR" and "SR" represent that the pressure gradients are calculated from true and reconstructed distributions respectively. β in Eq. (2) is a dynamic coefficient used to balance the weight of the gradient term. In the whole training process, the proportion of gradient loss term in total loss is continuously monitored epoch by epoch. Aiming at learning the gradient information fully, we control β value dynamically to ensure that the gradient loss accounts for more than 50% of the total loss. Once the proportion is less than 0.5, the β is automatically increased by 1% in the next epoch, until the proportion is no less than 0.5 again. In our recent study, the pressure fields were reconstructed based on the SRCNN with only L_{MSE} (Cao et al., 2022a). We found that the distribution characteristics of local extreme pressure could not be well reproduced. Therefore, in this study, we add $L_{gradient}$ to expect the gradient-guided SRCNN model to deal with the non-uniform measurement distribution in the facade tile, and to better capture local extreme pressure variations to improve the performance of peak pressure prediction.

To minimize the total training loss, the networks are trained using the Adam optimizer. The key hyperparameter settings are shown in Table 1. In Appendix B, we further explain how to determine the key hyperparameters for our SRCNN training. Early stop technique is applied in the training with a patience of 10. The main role of this technique is to find the right balance between underfitting and overfitting by stopping the training process. In Fig. 7, the training and validation losses are plotted versus the training epochs, when 10000 training samples are applied. Early stop is conducted once the validation loss cannot be reduced within 10 training epochs.

4. Results and discussions

In this section, since the negative pressure is the primary cause of cladding panel destruction, we first verify the applicability of pressure gradient guided SRCNN model in terms of the pressure prediction at the wind directions leading to extreme suction events, i.e., Tile A at $\alpha = +10^\circ$ and Tile B at $\alpha = 180^\circ$ in the wind tunnel experiment (Lamberti et al., 2020). Subsection 4.1 validates the ability of SRCNN to reconstruct instantaneous, time-averaged and RMS high-resolution pressure fields using coarse measurements. In the following two subsections, the wind pressure peaks are estimated over the area of a glazed panel. In the last section, the effect of various typical wind directions on the performance of pressure estimation of SRCNN constrained by gradient loss is discussed.

4.1. Prediction of pressure distributions

Fig. 8 present the instantaneous pressure coefficient (C_p) distributions on Tile A at $+10^\circ$ and on Tile B at 180° reconstructed by SRCNN with $L_{gradient}$ constraint, compared with super-resolution distributions reconstructed without $L_{gradient}$ constraint and the real high-resolution snapshots at the same instant within the time series of testing dataset. The instants when the evident suctions were observed near the tile corner and edge in PoliMi test are selected on Tile A and B for comparison, respectively. As shown in Fig. 8(a)–(c), as the pressure gradient are embedded, the distribution characteristics of extreme suctions are captured more precisely at the top corner of the Tile A, approaching to the real snapshot. Fig. 8(d)–(f) illustrates the prominent negative pressure zone in the bottom of Tile B can be better reproduced in magnitude when the $L_{gradient}$ is added, compared with the reconstructed distribution without the gradient constraint.

Based on 10000 training samples from each wind direction, Fig. 9(a)-(d) show the time-averaged pressure coefficient ($\overline{C}_p$) distributions reconstructed by the SRCNN model trained with $L_{gradient}$ term, in comparison of the true $\overline{C}_p$ statistics within the testing period of $t = 0$–3828 s. On Tile A, as shown in Fig. 9(a) and (b), the snapshot contours are not perfectly smooth which may be induced by the unstable three-dimensional vortices near the top corner of the facade. Nevertheless,

Table 1
Main hyperparameters for SRCNN model training.

Hyperparameters	Values
Learning rate	10^{-4}
Batch size	16
Tolerance	10
Residual block layers	16
Kernel size	3×3

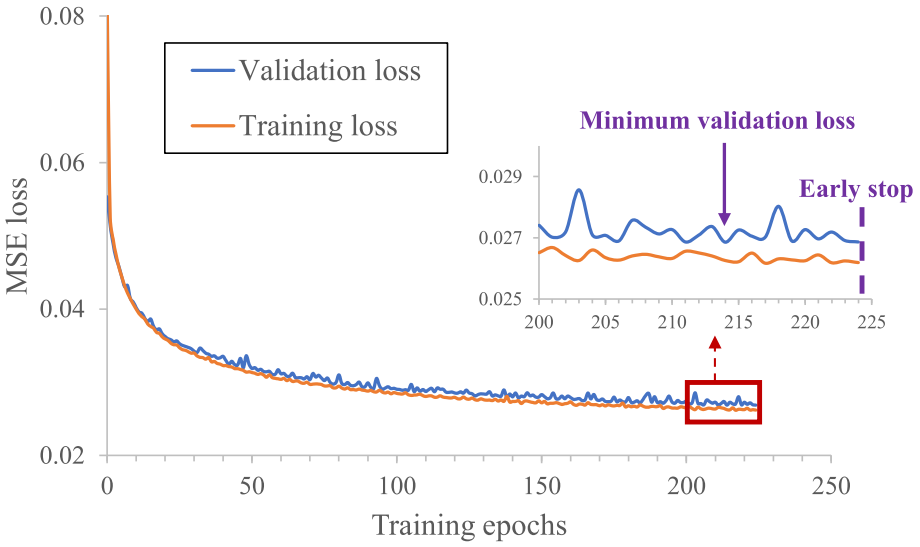

Fig. 7. Training and validation losses versus the training epochs. The attached figure explains the implementation of the early stop.

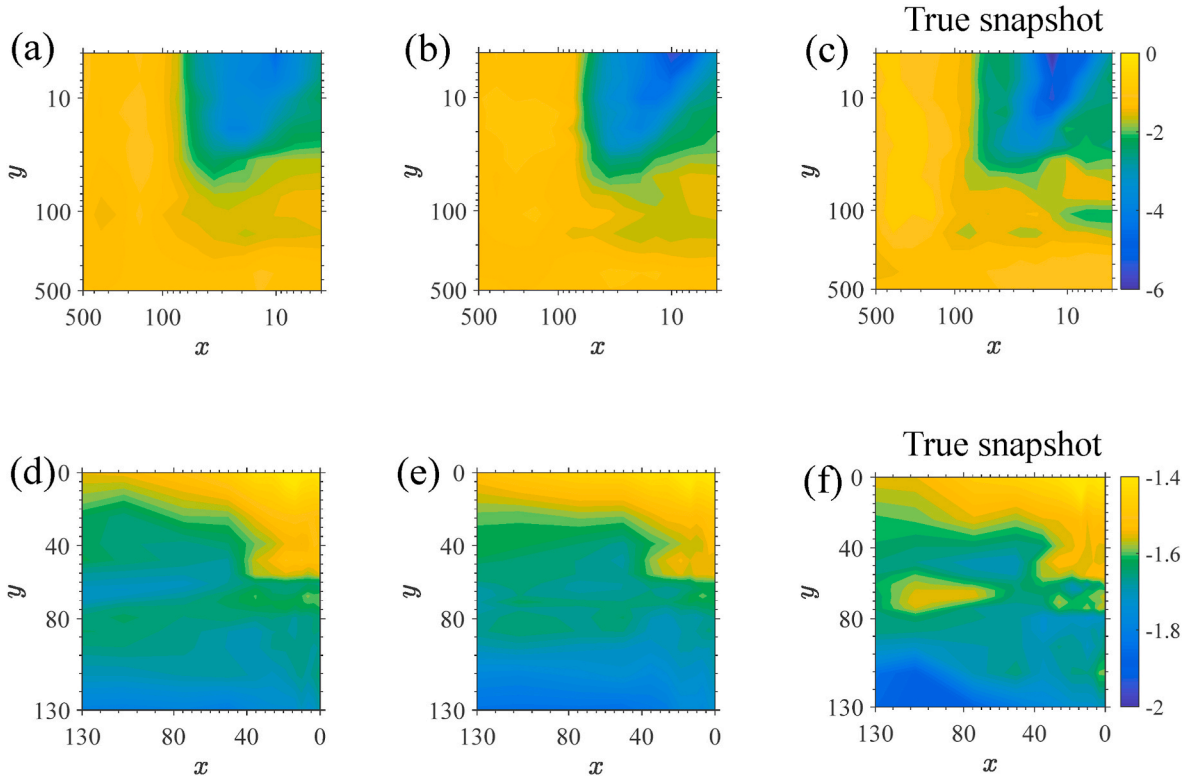

Fig. 8. Instantaneous C_p distributions reconstructed by SRCNN model (a) (d) without and (b) (e) with $L_{gradient}$ constraint as 10000 training samples are extracted from each wind direction, compared with (c) (f) the true distribution on Tile A (top row) when $\alpha = +10°$ at $t = 17.5$ s (full-scale) and Tile B (bottom row) when $\alpha = 180°$ at $t = 33.9$ s (full-scale) in testing time series.

the authors believe the unsmooth contour will not significantly influence the discussions of SRCNN performance. The model reproduces a $\overline{C}_p$ distribution capturing the similar spatial features to the true statistics. Compared with the true $\overline{C}_p$ over Tile A, that over Tile B shows a significant two-dimensional distribution with smaller spatial variations at $\alpha = 180°$ as presented in Fig. 9(c) and (d). The shear-layer separation might occur on Tile B, while a small vortex is likely to form downstream of the frontal edge as observed by Cao et al., 2019, 2022b. Under the above flow regime, the SRCNN model can excellently reproduce the distribution characteristics of the $\overline{C}_p$ on Tile B.

As shown in Fig. 10, the reconstructed RMS pressure coefficient (C'_p) distributions on Tile A at 10° and Tile B at 180° are compared with the true RMS fields within the testing time histories. The reconstructed fields are trained by SRCNN without and with $L_{gradient}$ constraint, based on 10000 training samples extracted from each wind direction. At the top corner of Tile A at 10°, the strong fluctuations in the pressure time series can be reproduced more successfully with $L_{gradient}$ constraint, as presented in Fig. 10(a)–(c). On Tile B at 180°, as the SRCNN are trained with $L_{gradient}$ constraint, the reconstructed C'_p filed is quantitatively higher than the one reconstructed from $L_{gradient}$ missing SRCNN, and

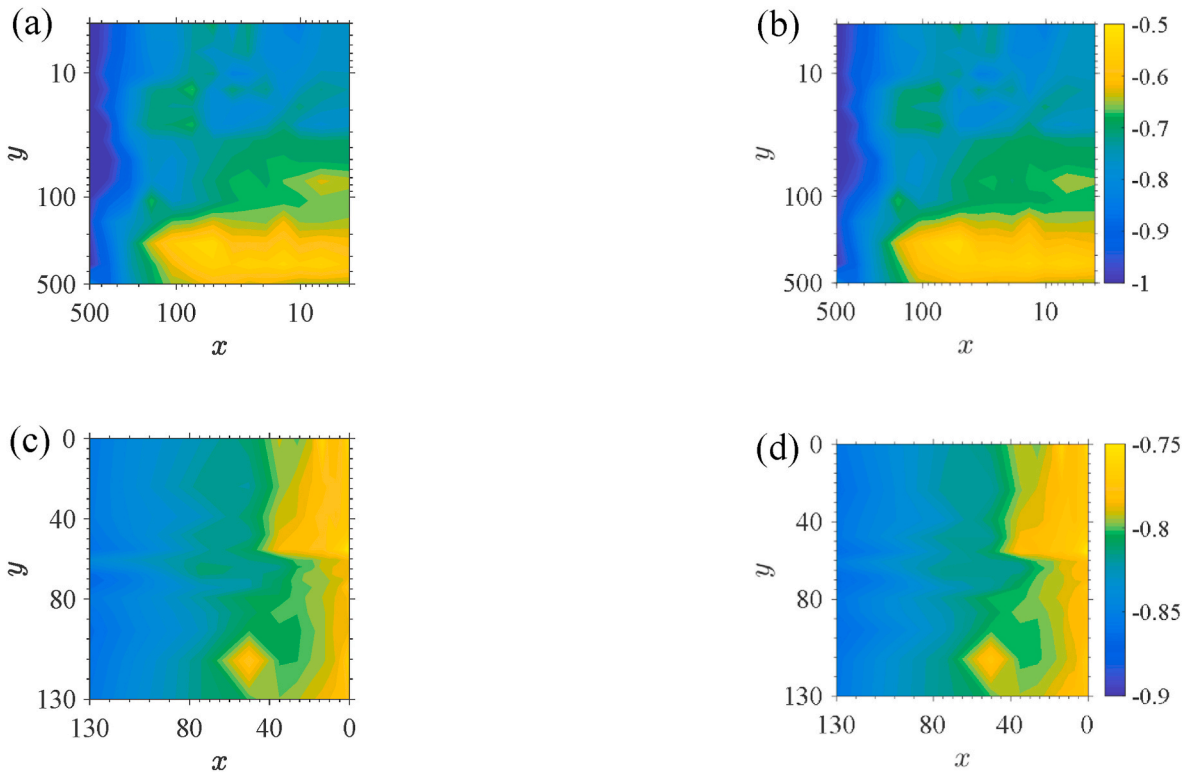

Fig. 9. Time-averaged $\overline{C}_p$ distributions reconstructed by (a) (c) $L_{gradient}$ constrained SRCNN model with 10000 training samples from each wind direction, compared with (c) (d) the true averaged fields for Tile A (top row) when $\alpha = +10^{\circ}$ and Tile B (bottom row) when $\alpha = 180^{\circ}$.

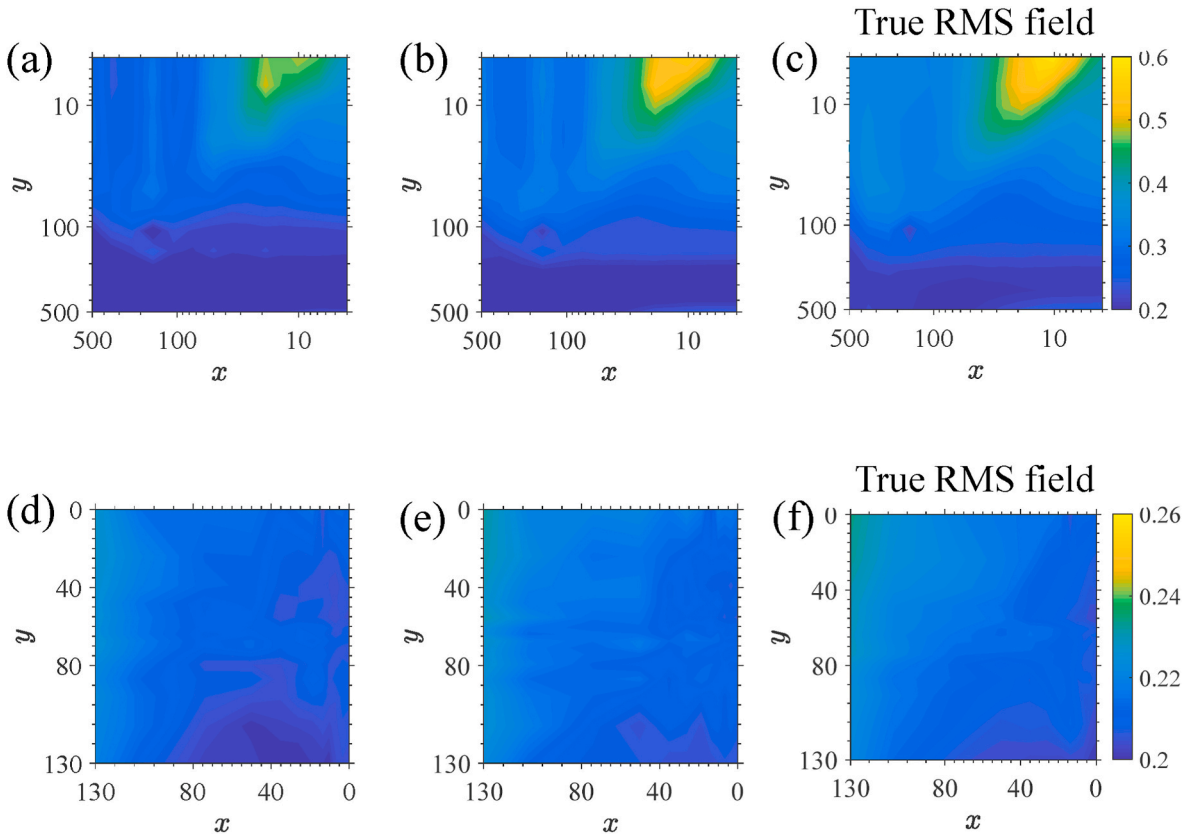

Fig. 10. RMS C'_p distributions reconstructed by SRCNN model (a) (d) without and (b) (e) with $L_{gradient}$ constraint as 10000 training samples are extracted from each wind direction, compared with (c) (f) the true distribution on Tile A (top row) when $\alpha = +10^{\circ}$ at $t = 17.5$ s (full-scale) and Tile B (bottom row) when $\alpha = 180^{\circ}$.

qualitatively more similar with the true distribution in Fig. 10(d)–(f), when the extracted samples reach 10000 from each wind direction.

In Appendix A, we further discuss the dependences of the errors and precisions of the instantaneous and RMS pressure reconstructed by SRCNN on the number of training samples. We discover that when the training samples reach 10000 from each wind direction, the pressure reconstruction of SRCNN with and without $L_{gradient}$ constraint both enter convergent stages and achieve relative lower errors and higher accuracies for both tiles at wind directions prone to extreme suctions. Based on certain training sample sizes (sampling frequencies), embedding pressure gradients are expected to improve reconstruction performance further.

4.2. Analysis of peak area-averaged pressure

To evaluate the estimation performance of the present machine learning method, the predicted peak area-averaged pressure coefficients obtained by the SRCNN model are compared with the true results and the predictions of the traditional TVL approach over the areas of glazed panels. The analysis will pay attention to the panel regions near the top corner on Tile A and close to the edge at the mid-height on Tile B, as indicated in Fig. 11(a) and (b). Two sizes of square panels, i.e., 1.5 m × 1.5 m and 3 m × 3 m at full-scale or 30 mm × 30 mm and 60 m × 60 mm at model scale, are considered on each tile. These regions were concluded to encounter highly negative or positive pressure events by Lamberti et al. (2020) and Pomaranzi et al. (2022). Therefore, a relatively high spatial resolution of pressure taps was installed there to better capture the local extreme pressure so that the 'true' area-averaged pressures could be estimated more accurately in their wind tunnel tests. Once the panel size becomes even larger, the mean installation density of measuring taps is sparser. It means the area-averaged pressures integrated from the pressure measurements become less accurate and are insufficient to be used as the reference bases for verification.

Based on the pressure fields reconstructed from the low-resolution pressure values through the SRCNN model, the super-resolution area-averaged pressure coefficient ($C_{p,\ SR}$) over the panel area is calculated according to Eq. (5). The spatial average pressure coefficients based on the low-resolution input data ($C_{p,\ LR}$) and true high-resolution measurements ($C_{p,\ AA}$) are defined by Eq. (5) as well for comparison. The $C_{p,\ SR}$, $C_{p,\ LR}$ and $C_{p,\ AA}$ are all represented by $C_{p,\ Area}$ in Eq. (5):

$$C_{p,Area}(t) = \frac{\sum_{i=1}^{N} C_{p,i}(t) A_i}{A}, \tag{5}$$

where $C_{p,\ i}$ denotes the pressure coefficient recorded or predicted at the ith tap, A_i is its tributary area and A is the total area of the panel. Each boundary of a tributary region is the vertical bisector of the line connecting the two adjacent pressure taps. The time-filtered pressure coefficient ($C_{p,\tau}$) is obtained by time-averaging the raw coefficient time-histories at an individual pressure tap to represent area-averaged coefficient within the panel region. The time span of the moving average window τ is determined based on the TVL equation of Eq. (1), with L being the diagonal of the panel while V representing the reference velocity at the building height. The constant K is varied in the range of [0, 5]. In this study, considering that the optimal K may be varied according to the wind direction conditions, K = 0.0, 1.0, 2.0, 3.0, 4.0, 4.5 and 5.0 including the Holmes (1997) (K = 1.0) and the Lawson formulation (Lawson, 1976) (K = 4.5) are adopted. Correspondingly, full-scale values of τ are summarized in Table 2. The pressure time series at the taps approaching to the building edges (E), near the center (C) and far from the edges (F) are time-filtered in each size of panel to estimate the $C_{p,\ AA}$ values, that is, E_1, C_1 and F_1 on the 1.5m × 1.5m panel and E_2, C_2 and F_2 on the 3m × 3m panel in Fig. 11 are analyzed by TVL method on Tile A and B, respectively. In addition to the TVL estimation, we also calculate the pneumatic-averaged pressure coefficient, $C_{p,\ pa}$, to compare the prediction accuracy with $C_{p,\ SR}$. The $C_{p,\ pa}$ is obtained by averaging the pressure signals from 5 pressure taps on each panel, one near the panel center and the other four approaching to four corners respectively, as shown in Fig. 12.

Fig. 13 first compares the time histories of the $C_{p,\ SR}$ obtained by $L_{gradient}$ embedded SRCNN based on 40000 training samples (10000 from each wind direction) and $C_{p,\tau}$ generated by Holmes formulation (K = 1) with those of the $C_{p,\ AA}$ in each size of panels on Tile A at $\alpha = +10°$ and Tile B at $\alpha = 180°$. We focused on the certain periods with maximum negative peaks in the whole testing time series. The $C_{p,\ SR}$ curves exist better agreements in terms of the trends and peaks with $C_{p,\ AA}$ than the TVL results in four sets of data. Besides, three $C_{p,\tau}$ curves change severely dependent on the selected time-filtering locations. On Tile A at $\alpha = +10°$, the $C_{p,\tau}$ processed at the top corner of two panels present clear underestimations relative to the $C_{p,\ AA}$ while the overestimations would appear at the tap far from the edges. On Tile B at $\alpha = 180°$, the $C_{p,\tau}$ near the centers in both panels substantially overestimate the $C_{p,\ AA}$ peak pressure while the underestimated results would be obtained by the

Table 2
Full-scale values of τ [s] for different panel sizes and K values.

Panel size	$K = 0$	$K = 1$	$K = 2$	$K = 3$	$K = 4$	$K = 4.5$	$K = 5.0$
1.5 m × 1.5 m	0	0.08	0.15	0.23	0.31	0.35	0.39
3 m × 3 m	0	0.15	0.31	0.46	0.62	0.69	0.77

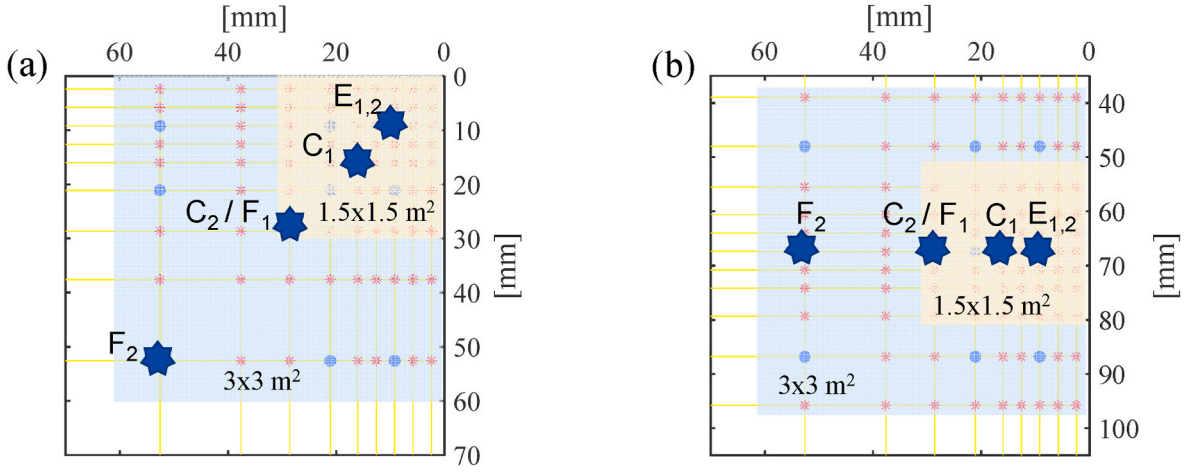

Fig. 11. Square panels of different sizes on (a) Tile A and (b) Tile B. TVL predicted results at E_1, C_1 and F_1 on the 1.5m × 1.5m panel shown by yellow color and E_2, C_2 and F_2 on the 3m × 3m panel shown by blue color are analyzed.

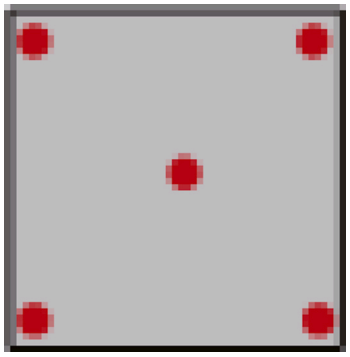

Fig. 12. Configurations considered for the pneumatic-averaged pressure.

other taps. Unfortunately, for each tile, there is no tap location providing more precise predictions of pressure peaks than others, as the panel size is varied.

In this study, the estimation accuracies of pressure peaks for various prediction approaches can be quantitatively determined by the mean difference rates, which is averaged over different moments when the peak pressure occurs. At each moment, the difference rate is computed from the errors between the predicted and true values of peak area-averaged pressures over the panels, divided by the true peak pressures. During the testing period, Table 3 shows the mean difference rates of the extreme negative $C_{p,\ SR}$ peaks relative to the negative $C_{p,\ AA}$ peaks in 1.5 m × 1.5 m and 3 m × 3 m panel on Tile A and B respectively, based on SRCNN model without and with $L_{gradient}$ constrained. The rates of $C_{p,\ LR}$ are also included for comparative analysis. The coefficients −2.8 and −2.3 are set as the thresholds for $C_{p,\ AA}$ in 1.5m × 1.5m and 3m × 3m panels on Tile A respectively, and the threshold of $C_{p,\ AA}$ is determined as −1.5 for each panel size on Tile B. Once the above thresholds are selected, 20–30 $C_{p,\ AA}$ peaks are guaranteed to be involved in the comparison with the predicted peaks for different panel sizes on each tile.

As seen from Table 3, when 10000 training samples are applied from each wind direction without the loss term of pressure gradient, the prediction errors of $C_{p,\ LR}$ and $C_{p,\ pa}$ are approximately 2–4 times of those of $C_{p,\ SR}$. This illustrates that the super-resolution method predicts a more accurate peak spatial averaged pressure compared with the direct integration from the sparse pressure points. The reason why the prediction precisions are improved lies in the advantage of the SRCNN. The model is good at extracting local distribution features in a small spatial range. When it is used for super-resolution of pressure measurements, the local distribution information of extreme pressure is expected to be better reproduced by denser pressure data, so as to more accurately characterize the average extreme pressure over the panel. When employing the same sample size with pressure gradient loss, the prediction errors decline further. Especially for Tile A where the spatial variation of local suction values is more severe, the degree of error

Table 3
Mean difference rates of peak negative values of $C_{p,\ LR}$ calculated from low-resolution fields, $C_{p,\ pa}$ calculated from five-tap configuration and $C_{p,\ SR}$ obtained by super-resolution fields without and with pressure gradient constraint, in comparison with those of $C_{p,\ AA}$ on the panels of two sizes on Tile A when $\alpha = +10°$ and Tile B when $\alpha = 180°$.

Tile	Panel size	$C_{p,\ LR}$	$C_{p,\ pa}$	$C_{p,\ SR}$ (without $L_{gradient}$)	$C_{p,\ SR}$ (with $L_{gradient}$)
Tile A at $\alpha = +10°$	1.5 m × 1.5 m	17.01%	30.04%	7.88%	6.30%
	3 m × 3 m	10.55%	20.27%	6.53%	6.12%
Tile B at $\alpha = 180°$	1.5 m × 1.5 m	7.30%	8.48%	2.11%	1.92%
	3 m × 3 m	4.07%	4.84%	1.51%	1.38%

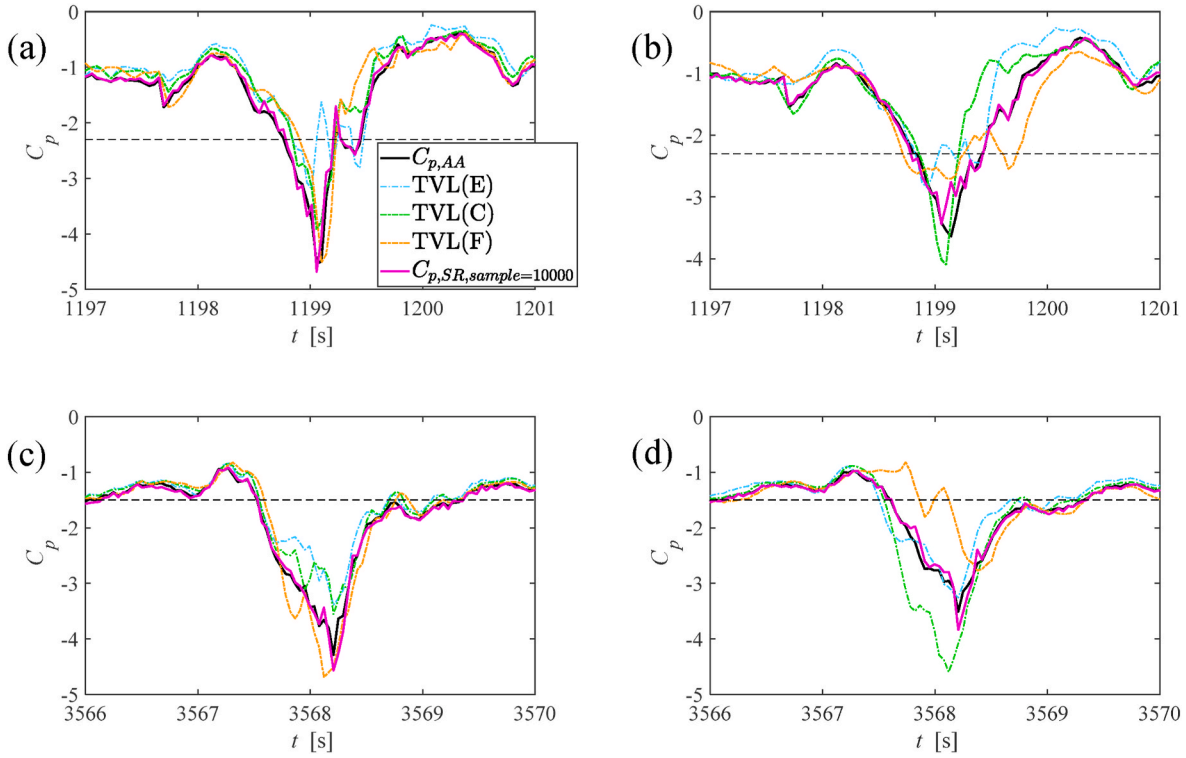

Fig. 13. Comparison between the pressure variations of $C_{p,\ AA}$, $C_{p,\ SR}$ and $C_{p,\tau}$ with $K = 1.0$ in (a) 1.5 m × 1.5 m and (b) 3 m × 3 m panel on Tile A at 10° and (c) 1.5 m × 1.5 m and (d) 3 m × 3 m panel on Tile B at 180° as the maximum negative $C_{p,\ AA}$ occurs. The thresholds are set to extract the $C_{p,\ AA}$ peaks for comparisons, which are denoted by the black dash lines.

reduction is more obvious than that in Tile B. Combined with the results depicted in Subsection 4.1, it illustrates that the super-resolution method considered the gradient constraint can better position the local extreme values and characterize the gradient variations, which gives a chance to provide more accurate predictions for area-averaged peak pressure.

As shown in Fig. 14, for the wind directions leading to extreme suctions, the mean difference rates from the gradient-guided SRCNN model keep steady and are apparently lower than the TVL results of all tap positions and K factors analyzed, when 6000, 10000 and 60000 samples are extracted from each training wind direction. It implies that the gradient-guided SRCNN provides higher accuracy and stronger robustness in the estimation of negative pressure peaks than the TVL method. According to Table 3 and Fig. 14, the general prediction accuracies of $C_{p,\ SR}$ are higher on Tile B at 180° in comparison with the results on Tile A at +10°. It is attributed to the stronger spatial correlation of true pressure distribution on Tile B. As stronger suctions and more complex pressure distributions occur, it becomes more difficult to capture the peak pressures on Tile A.

4.3. Analysis of design peak wind pressure

Surry and Djakovich (1995) put forward that the reliable statistics of wind pressure should be carry out in a sufficient time series. In practical engineering, it is usually impossible to conduct the statistical analysis of pressure peaks only by relying on wind tunnel data within limited test durations, owing to cost and technical constraints. Therefore, assuming the distribution as Fisher-Tippet Type 1, Cook-Mayne method (Cook and Mayne, 1980) was adopted to calculate the extreme pressure coefficients of 78% non-exceedance probability for the building facades (Hui et al., 2013; Kim et al., 2012). In this study, we employ the simplified Cook-Mayne method to obtain the design values of the peak pressure as well. The total test duration is divided into 6 groups corresponding to six 10 min-long data groups at the full scale. The design pressure value $\widehat{C}_p$ with 78% quantile is expressed as Eq. (6):

$$\widehat{C}_p = m \mp 0.636 \cdot \sigma, \tag{6}$$

where m and σ are the mean and RMS values of the extreme pressure values from 6 sample groups. When the design negative or positive pressure is estimated, a minus or plus sign is used in Eq. (6) respectively before the term with σ.

As displayed in Fig. 15, on both tiles, the relative difference rates of the $\widehat{C}_p$ based on the gradient-missing SRCNN model are evidently lower than mean ones in TVL approach averaged over different selections of time-filtering locations and K factors. Furthermore, the errors provided by the gradient-guided SRCNN model have even less magnitudes than the ones predicted by gradient-missing SRCNN model. It demonstrates that the current gradient-guided method offers more accurate and credible estimations for design extreme pressure.

4.4. Analysis of peak pressures at different typical wind directions

The wind pressure modes and flow patterns on the building facades are greatly dependent on the variation of the wind directions. In this subsection, the cases of several typical wind directions are investigated to reveal the effect of pressure modes on the performances of peak pressure prediction by $L_{gradient}$ constrained SRCNN model.

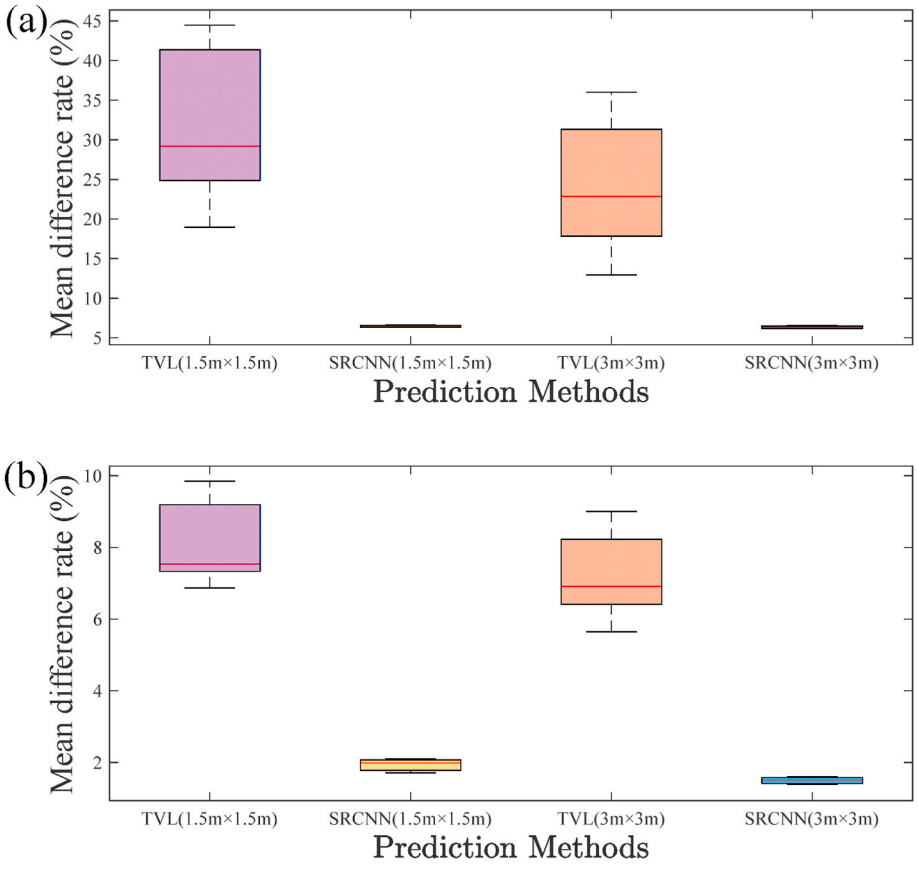

Fig. 14. Boxplots of the mean difference rates between peaks of $C_{p,\ AA}$ and the prediction values obtained by the TVL approaches and gradient-guided SRCNN models based on 6000, 10000 and 60000 samples extracted from each training wind direction, when different panel sizes are considered on (a) Tile A at 10° and (b) Tile B at 180°.

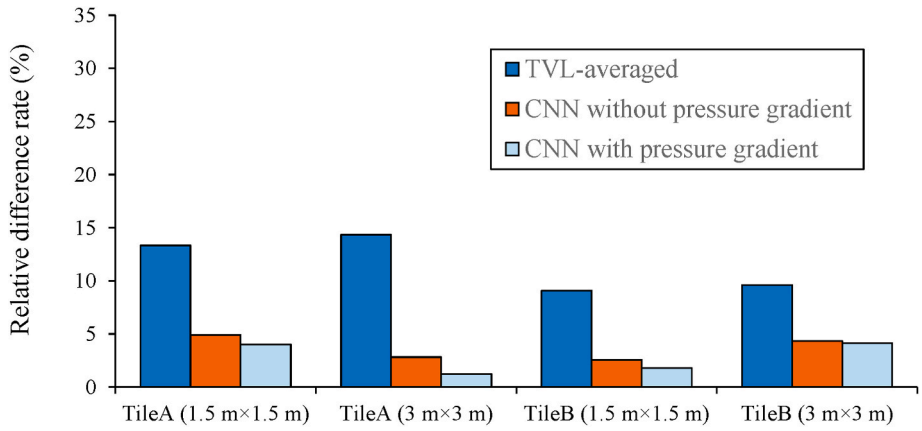

Fig. 15. Relative difference rates of design $\widehat{C}_p$ values predicted by SRCNN without and with pressure gradient constraint, compared with the mean errors in TVL approach averaged over different selections of time-filtering locations and K factors: on Tile A at 10° and on Tile B at 180°.

4.4.1. Selection of the analyzed wind directions

The investigated wind directions are selected according to some typical pressure modes generated on the two critical tiles analyzed above. On both tiles, the high-resolution distributions of the time-averaged pressure in PoliMi experiment are displayed at different wind directions in Fig. 16.

At a small wind direction of $\alpha = -15°$, two tiles are located at the downstream portion of the side facade which is characterized by the flow separation and reattachment. In Fig. 16(a) and (d), it can be found that the less negative $\overline{C}_p$ regions are formed at the bottom left of Tile A and left portion of Tile B. The presence of the shear-layer reattachment at $-15°$ is assumed to make the $\overline{C}_p$ values in above regions relatively higher (Keerthana and Harikrishna, 2017).

At $\alpha = -170°$, two tiles are located just downstream the leading edge of the flow-reattachment facade. As shown in Fig. 16(b), a significant negative $\overline{C}_p$ region is formed near the free end of the building on Tile A. It might be associated with a standing conical vortex observed by Okuda and Taniike (1993) that accounts for the low time-averaged surface pressure. An extreme suction zone vertically passing through Tile B is presented in Fig. 16(e). This kind of the $\overline{C}_p$ trough was reported by Cao et al. (2022b) in regions downstream the leading edge, which may be an indicator of a spanwise edge vortex arisen from the flow separation.

At $\alpha = -150° \sim -135°$, the two tiles might be subject to strong flow impingements in the windward conditions. In Fig. 16(c), the negative $\overline{C}_p$ zones appear at two top corners on Tile A at $\alpha = -150°$. Considering that the $\overline{C}_p$ values are approaching to zero around the corner region as the wind direction is rotating toward $\alpha = -135°$, it is more appropriate to conduct the following predictions of peak negative pressures in the case of $\alpha = -150°$. However, similar $\overline{C}_p$ distributions on Tile B are discovered between the cases of $\alpha = -135°$ and $\alpha = -150°$ in PoliMi test. Compared with the case at $\alpha = -150°$, the positive $\overline{C}_p$ values are more dominant over the area of Tile B at $\alpha = -135°$, which would be a better benchmark

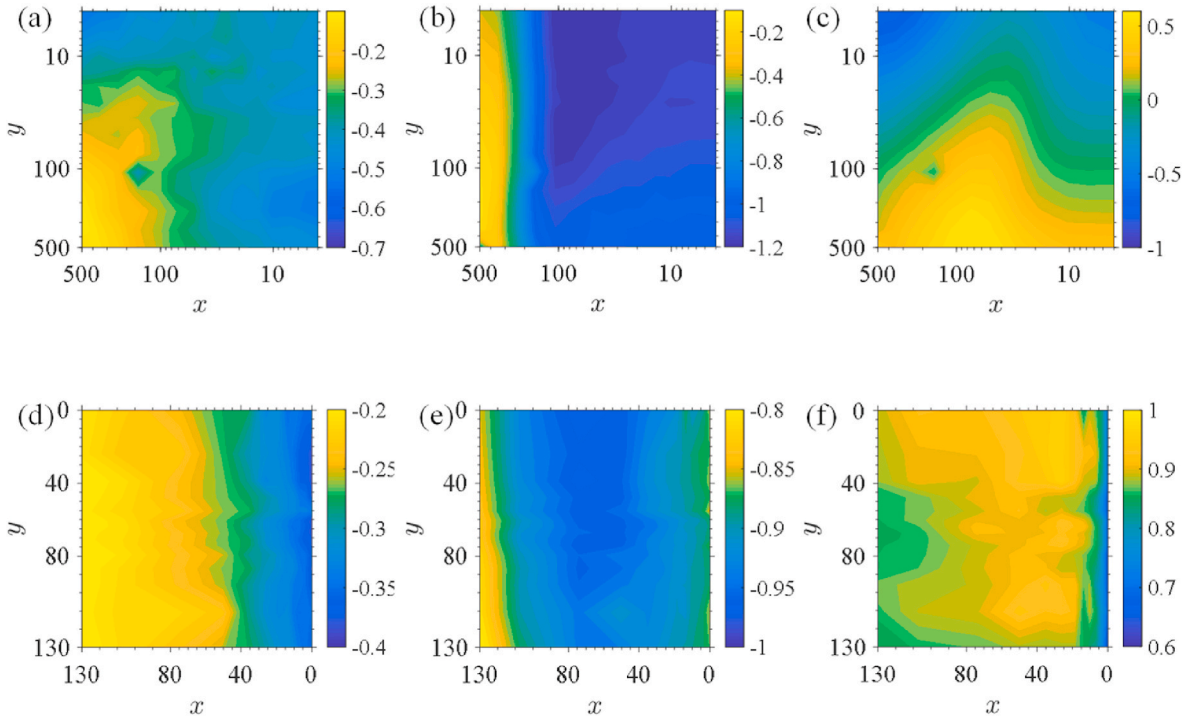

Fig. 16. Time-averaged $\overline{C}_p$ distributions in PoliMi experiment at (a) $\alpha = -15°$, (b) $\alpha = -170°$ and (c) $\alpha = -150°$ on Tile A and at (d) $\alpha = -15°$, (e) $\alpha = -170°$ and (f) $\alpha = -135°$ on Tile B.

for the following analysis of positive pressure prediction.

According to the detailed analyses and screening at different wind directions, we choose the typical pressure and near-wall flow modes to verify the general applicability of SRCNN prediction. Specifically speaking, the selected conditions include the downstream portion of flow separation-reattachment wall (i.e., $\alpha = -15^\circ$ for both tiles), the upstream portion of flow separation-reattachment wall (i.e., $\alpha = -170^\circ$ for both tiles), and the windward wall of strong flow impingement (i.e., $\alpha = -150^\circ$ for Tile A and $\alpha = -135^\circ$ for Tile B).

4.4.2. Comparison of peak area-averaged pressure

Across various α cases, we apply the indicator of the mean difference rate (or mean relative error) to statistically assess the prediction accuracy of $C_{p,\ AA}$ peaks by SRCNN.

Focusing on the SRCNN model with 10000 training samples, Fig. 17 shows the histograms of the mean difference rates between peaks of $C_{p,\ SR}$ and $C_{p,\ AA}$ across all wind directions, along with the those between peaks of $C_{p,\tau}$ and $C_{p,\ AA}$. Among different selections of time-filtering locations and K factors in each size of panel, the minimum mean difference rates of TVL estimations are chosen for comparison. On both tiles at all analyzed α, it is found that the mean difference rates of $C_{p,\ SR}$ are below 6% and even lower than the most accurate TVL estimations over all considered taps and K factors. Compared to those at all other wind directions on Tile A, the overall difference rates at $\alpha = -150^\circ$ are even higher, as presented in Fig. 17(a). It is possibly because the frequent alternations of negative and positive pressure peaks appear around the top corner on Tile A, which hinders the accuracy improvement in the prediction of the negative peaks. Conversely, at $\alpha = -135^\circ$, the steady windward loadings on Tile B make it easier for prediction of extreme positive pressure. So deservedly, relatively lower prediction errors are displayed in Fig. 17(b). Moreover, since the more significant suctions or spatial pressure variations are localized in a smaller area near the edges, the prediction precisions of peak area-averaged pressure by SRCNN model are slightly higher in 3m × 3m panels than those in 1.5m × 1.5m panels in most conditions. Exceptionally, for Tile A at $\alpha = -150^\circ$, a restrained area characterized by frequent negative peaks as present in Fig. 15(c). It is speculated that this area might make great contribution to the generation area-averaged suction over a large panel region. the SRCNN model presents the relatively worse estimations of the peak negative pressure in the larger panel.

Fig. 18 exhibits that the minimum sample size with which the SRCNN model can obtain the mean difference rates of $C_{p,\ SR}$ peaks below 50% of those of $C_{p,\tau}$ predicted by the TVL approach at various wind directions. The mean difference rates of $C_{p,\tau}$ here have been averaged over different selections of time-filtering taps and K factors. The figure is an indicator to determine how much training cost of the SRCNN is required to realize the ideal prediction performance at each wind direction.

When the flow reattachments occur at $\alpha = -15^\circ$ on both tiles, as not less than 1000 training samples from each wind direction are used, the estimation errors produced by the machine learning method are less than 50% of the average errors from TVL approach. Similar observations are present on Tile A dominated by the conical vortex ($\alpha = -170^\circ$) and Tile B in the windward conditions ($\alpha = -135^\circ$). Nevertheless, when the positive-negative alterations of peak pressures are recognized at the corner of Tile A ($\alpha = -150^\circ$) and the strong edge vortices are formed near Tile B ($\alpha = -170^\circ$), only the SRCNN with larger sample size (exceeding 10000 from each wind direction) could provide obviously more realistic and steady representations of $C_{p,\ AA}$ than the TVL predictions. In general, weaker influence of the vortices and stronger correlation of pressure distributions on the tiles contribute to predicting more accurate extreme pressure with less training samples for SRCNN. Across all typical wind directions, the present machine learning method exhibits stronger precision and robustness in estimation of peak pressure than the traditional TVL approach.

4.4.3. Analysis of design peak wind pressure

Fig. 19 indicates the relative difference rates of design $\widehat{C}_p$ values predicted by $L_{gradient}$ constrained SRCNN at different wind directions, compared with the mean values of those predicted in TVL approach averaged over different selections of time-filtering locations and K factors. At $\alpha = -15^\circ$ on both tiles and $\alpha = -170^\circ$ on Tile A, the relative errors of the design $\widehat{C}_p$ values based on the SRCNN model are successfully diminished versus average ones from the TVL approach when only 4000 training samples (1000 from each training wind direction) are employed, as shown in Fig. 19(a) and (c). Whereas, on Tile B at $\alpha = -170^\circ$, the prediction errors of SRCNN with 1000 samples lie in the higher levels than the TVL results, as presented in Fig. 19(c). It is probably because Tile B encounter stronger edge vortices at -170° than the other wind direction cases and thus its peak pressure modes should be properly learned by SRCNN with more training samples. Indeed, the relative errors of the $\widehat{C}_p$ based on the SRCNN model experience evident drop on both tiles to less than 2% as those in other α cases behave, when more training samples (40000) are applied (Fig. 19(d)). These low errors reflect superior estimations of SRCNN model than the TVL method.

In terms of the windward conditions for Tile A, especially in 1.5 m × 1.5 m panel, the relative difference rates of SRCNN drop apparently as the sample size rises from 4000 to 40000, as presented from Fig. 19(a) and (b). Excellent prediction ability of the SRCNN model is shown with the error below 1%, much lower than the averaged TVL results. As the positive pressure prevails on the Tile B at $\alpha = -135^\circ$, it can be seen from Fig. 19(c) that the $\widehat{C}_p$ difference rates from SRCNN prediction remain below 1%, with only 1000 training samples from each wind direction. It indicates better predictions than other wind directions on the same tile. Because of the relatively uniform pressure distributions, the training sample size of the SRCNN has feeble effect on the prediction precisions of design $\widehat{C}_p$ values at this wind direction.

On the whole, at any wind directions discussed, the SRCNN models with 10000 samples from each wind direction have shown remarkable

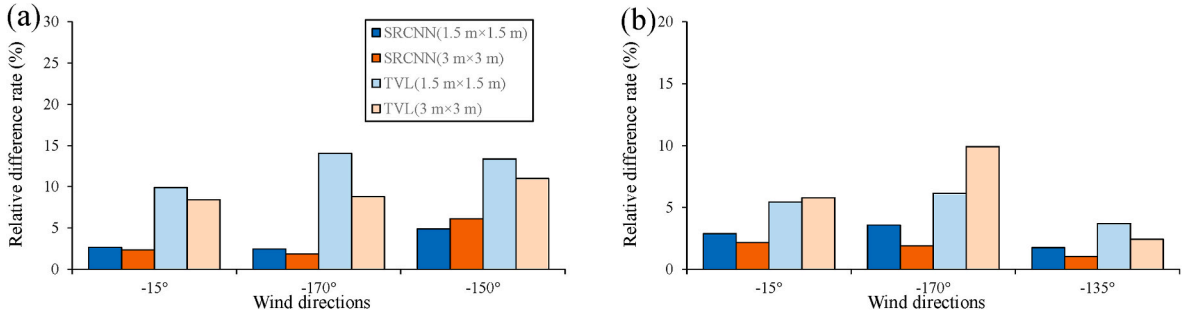

Fig. 17. Mean difference rates between peaks of $C_{p,\ AA}$ and the predicted peak values obtained by the TVL approaches and $L_{gradient}$ constrained SRCNN models based on 10000 training samples, when different panel sizes are considered on (a) Tile A at $\alpha = -15^\circ$, -170° and -150° and on (b) Tile B at $\alpha = -15^\circ$, -170° and -135°. The mean difference rates of TVL approach are the minimum ones among different selections of time-filtering locations and K factors in various sizes of panels.

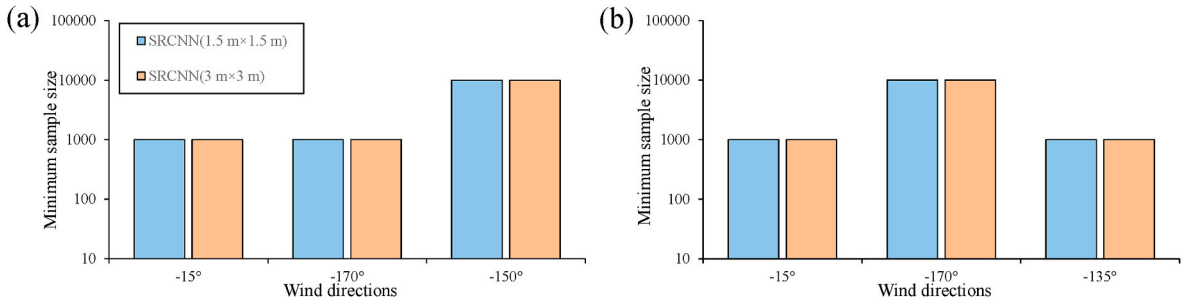

Fig. 18. Minimum sample size from each training wind direction with which the SRCNN model can obtain the mean difference rates of $C_{p,\ SR}$ peaks below 50% of those of $C_{p,\tau}$ predicted by the TVL approach at various wind directions, when different panel sizes are considered on (a) Tile A and (b) Tile B. The mean difference rates of TVL approach are also averaged over different selections of time-filtering locations and K factors in each size of panel.

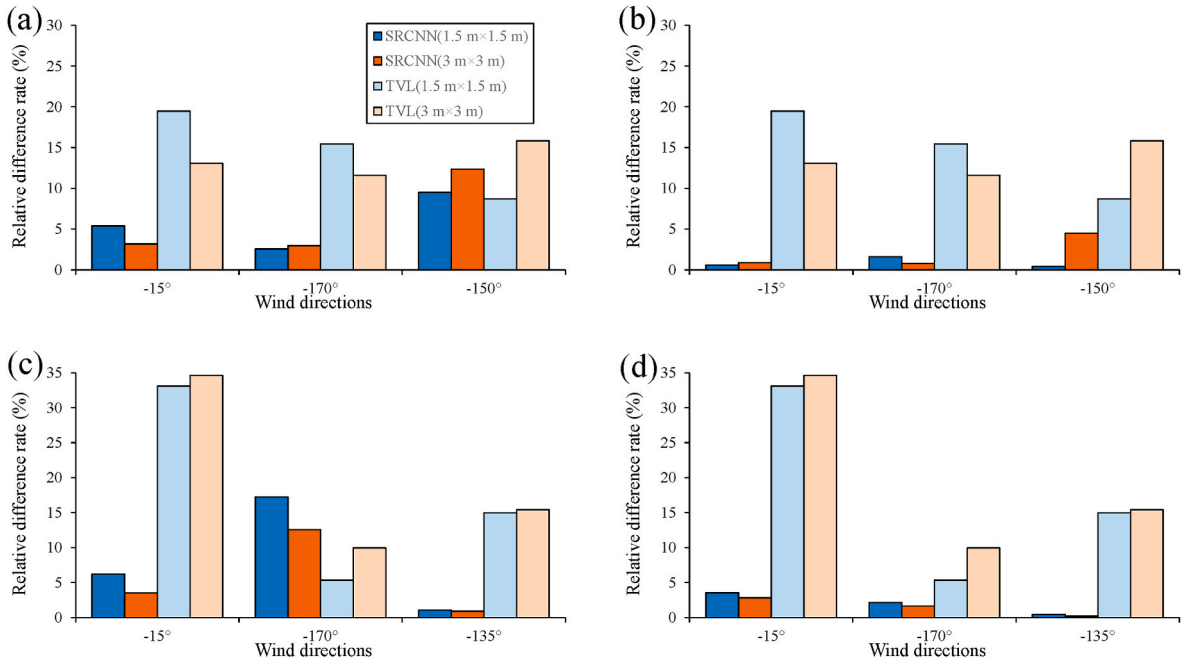

Fig. 19. Relative difference rates of design $\widehat{C}_p$ values predicted by SRCNN at various wind directions on Tile A based on (a) 4000 and (b) 40000 training samples and Tile B based on (c) 4000 and (d) 40000 training samples, compared with the mean values of those predicted in TVL approach averaged over different selections of time-filtering locations and K factors.

advantages over the TVL method in predicting extreme design pressure precisely.

5. Conclusions

To accurately evaluate peak pressure on cladding panels, SRCNN model is used to reconstruct the super-resolution pressure distributions from sparse measurement. We choose the high-resolution pressure database performed in the wind tunnel of PoliMi. In order to realize the generic prediction for various wind directions, we utilize pressure data from different incident angles beyond the predicting ones as the training dataset. The constraint represented by the pressure gradient are embedded in the loss function of the SRCNN. Two critical loading regions are focused near the top corners (Tile A) and edges (Tile B) of the lateral facade. In order to estimate the "true" peak area-averaged pressure coefficients ($C_{p,\ AA}$), the super-resolution pressure fields are integrated to obtain the reconstructed spatial average pressure coefficients ($C_{p,\ SR}$) within the cladding panel areas. The reconstruction and prediction of wind pressure consider the special configuration prone to extreme suction events and other three typical wind directions for each tile. After detailed discussions, the following conclusions can be drawn.

(1) Compared with the direct integrations from the sparse pressure data and the pneumatic-averaged coefficients based on 5-point configuration, the pressure peaks calculated from the super-resolution reconstructed distributions can represent the true area-averaged peaks more adequately, despite no pressure gradient loss embedded. Across all considered wind directions, the result shows that the higher precision of the SRCNN estimation compared to the traditional TVL approach. Additionally, the representative ability of the TVL method for the true spatial averaged pressure severely depends on the variations of filtering locations and the TVL factors. Relatively more steady predictions of peak pressures are provided by the SRCNN, showing its stronger robustness.

(2) When the SRCNN model is constrained by the pressure gradient loss, it can better capture the local extreme pressure regions and characterize the gradient variations. Based on more realistic pressure distribution, the SRCNN model can represent the true area-averaged peaks more adequately than the model without gradient loss.

(3) The incident angles and the corresponding flow patterns on the tiles have some effects on the prediction performance of the

gradient-guided SRCNN model. In the cases where flow reattachment ($\alpha = -15^{\circ}$) and flow impingement ($\alpha = -135^{\circ}$ on Tile B) occur, few training sample size (1000 training samples from each wind direction) could achieve evidently more precise predictions of pressure peaks for the SRCNN model, compared to those calculated from TVL signals on both tiles. In the other cases where the strong vortices (Tile A at $\alpha = +10^{\circ}$ and Tile B at $\alpha = 180^{\circ}$, -170°) or frequent alternations of positive-negative pressure peaks (Tile A at $\alpha = -150^{\circ}$) prevail, the credible prediction could only be obtained based on relatively larger sample size (exceeding 10000 training samples from each wind direction). It is revealed that the wind directions imposing less evident three-dimensional flow patterns and stronger correlation of pressure distributions contribute to predicting more accurate extreme pressure with less training resources for SRCNN.

(4) The design pressure $\widehat{C}_p$ values with 78% quantile calculated from different prediction methods are compared as well. It is also indicated that the SRCNN has a stronger spatial representative of peak pressures over a cladding panel than the time-filter signals, as handling all typical modes of pressure distributions. It should be noted that relatively higher prediction accuracies of design $\widehat{C}_p$ values tend to occur on Tile B in the windward conditions, which results from the relatively uniform pressure distributions on the middle height region of the building facade.

In summary, current SRCNN model exhibits a good applicability in peak pressure predictions of cladding panels affected by different flow patterns and pressure modes. In the future research, the applicability scope of machine learning methods is planned to be further extended. Firstly, in other wind tunnel experiments with sparse measurements, the trained SRCNN could be utilized as a direct or a transfer model to investigate and enhance its generalization performance of pressure reproduction. In other words, one can precisely reconstruct the high-resolution pressure distributions from new sparse data by employing the trained machine learning models or with much fewer high-resolution training samples. Secondly, the SRCNN method is expected to be practicable when the low-resolution measurements become sparser and further away from the facade edges of the building.

CRediT authorship contribution statement

Haokai Wu: Validation, Investigation, Visualization, Formal analysis, Writing – original draft. **Yaoran Chen:** Validation, Investigation, Visualization, Formal analysis. **Peixing Xie:** Formal analysis, Writing – review & editing. **Dai Zhou:** Investigation, Formal analysis, Supervision, Funding acquisition. **Tetsuro Tamura:** Methodology, Investigation, Supervision. **Kai Zhang:** Conceptualization, Visualization, Data curation. **Shuyang Cao:** Data curation, Supervision. **Yong Cao:** Conceptualization, Data curation, Writing – review & editing, Supervision, Funding acquisition.

Declaration of competing interest

The authors declare that they have no known competing financial interests or personal relationships that could have appeared to influence the work reported in this paper.

Data availability

The authors do not have permission to share data.

Acknowledgements

The research was funded by the National Natural Science Foundation of China (Grant No. 52108462 and No. 42306226), the Shanghai Sailing Program (Grant No. 21YF1419400), the Natural Science Foundation of Chongqing (Grant No. CSTB2023NSCQ-MSX0060), the Natural Science Foundation of Shanghai (Grant No. 21ZR1428900) and Shenlan Project of Shanghai Jiao Tong University (Grant No. SL2022MS004). The authors are grateful for the aerodynamic database, which was constructed by the research group led by Prof. Alberto Zasso at Politecnico di Milano (PoliMi).

Appendix A. Effect of training data size on the reconstruction precision of SRCNN

To quantitatively evaluate the reconstruction performance of the instantaneous pressure, the root mean square error (RMSE) and determination coefficient indexes (R^2) are computed for the reconstructed fields with 90000 time-steps:

$$\mathrm{RMSE} = \frac{1}{n} \cdot \sum_{j=1}^{n} \sqrt{\frac{1}{m} \sum_{i=1}^{m} (y_i - \widehat{y}_i)^2} \tag{7}$$

$$R^2 = \frac{1}{n} \cdot \sum_{j=1}^{n} \left[1 - \frac{\sum_{i=1}^{m} (y_i - \widehat{y}_i)^2}{\sum_{i=1}^{m} (y_i - \bar{y})^2} \right], \tag{8}$$

where y_i and $\widehat{y}_i$ stand for the observed and predicted pressure values at the ith tap respectively on Tile A or B at one instance, $\bar{y}$ is the mean value of the true pressure measurements at one snapshot. m and n are the numbers of the pressure taps and testing samples, respectively.

Fig. 20 (a) and (b) shows the RMSE errors and R^2 accuracies of reconstructed instantaneous pressure distributions on Tile A at $\alpha = +10^{\circ}$ and Tile B at $\alpha = 180^{\circ}$ within the testing time series, as a function of the training sample size from each wind direction. The curves show the reconstruction performance of SRCNN without $L_{gradient}$ informed. As the sample size is up to 10000, the reconstruction indexes become convergent, and the accuracy even decreases as the sample size is increased further for Tile B. The star signals denote the reconstruction errors and accuracies of SRCNN models constrained by $L_{gradient}$. On Tile A, the gradient embedded model has better reconstruction performance than the models without the $L_{gradient}$ constraint, as 10000 training samples from each wind direction are used. When the sample number further increases to 60000, the influence of embedding pressure gradient on the error and accuracy is weakened, as shown in Fig. 20(a) . On Tile B, as the sample size equals to 10000, the embedding of pressure gradient hardly effects the reconstruction accuracy of the SRCNN model. However, when the sample size becomes larger, the embedded $L_{gradient}$ leads to an improvement in the error and accuracy indexes, as shown in Fig. 20(b). In other words, the overfitting of the model will be alleviated, when the spatial variation characteristics of pressure gradient are considered in the training process.

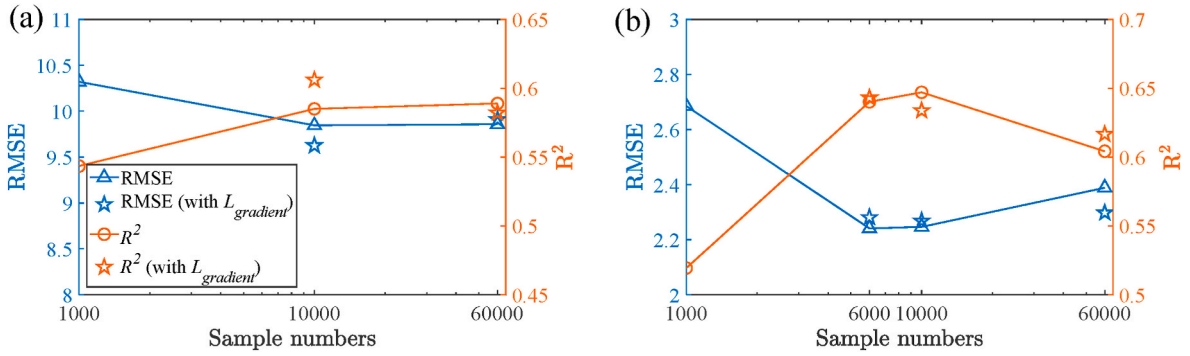

Fig. 20. Dependence of the RMSE errors and R^2 precisions of the instantaneous pressure reconstructed by SRCNN without $L_{gradient}$ embedded on the number of training samples, compared with the errors and precisions of $L_{gradient}$ embedded SRCNN at wind directions prone to extreme suctions for (a) Tile A at $\alpha = +10°$ and (b) Tile B at $\alpha = 180°$.

The variations of $\mathrm{RMSE_s}$ error and R_s^2 accuracy with the training samples are illustrated in Fig. 21(a) and (b) for the C_p' reconstructed by $L_{gradient}$ missing SRCNN on Tile A and B, respectively. The star signals represent $\mathrm{RMSE_s}$ and R_s^2 criteria of SRCNN models constrained by $L_{gradient}$. The two criteria of the pressure statistics over a testing period are defined as follow:

$$\mathrm{RMSE_s} = \sqrt{\frac{1}{m}\sum_{i=1}^{m}(y_i - \hat{y}_i)^2} \tag{9}$$

$$R_s^2 = 1 - \frac{\sum_{i=1}^{m}(y_i - \hat{y}_i)^2}{\sum_{i=1}^{m}(y_i - \bar{y})^2}, \tag{10}$$

where y_i and $\hat{y}_i$ are the statistics values of the measured and reconstructed pressure data at ith tap. The other symbols have the same meanings as Eqs. (7) and (8).

On Tile A, it is found from Fig. 21(a) that the accuracies of reconstructed C_p' show a slight decline trend, probably owing to the underestimation in C_p time fluctuations when the sample size rises to 60000. In view that Tile A is located at the top corner of the leeward facade at $\alpha = +10°$, the shedding vortices around the tile tend to unsteady, resulting in the aperiodic extreme suction peaks appearing at several taps. The increase of the sampling frequency of training samples possibly leads to overfitting of the model, that is, the model has learned too much redundant information from certain wind direction cases thus it is more difficult to perfectly generalize the extreme pressure fluctuations in the testing wind direction at some measuring positions. Herein, simply enlarging the sample size cannot significantly reduce the errors of reconstructed C_p'. When the $L_{gradient}$ is informed in SRCNN, the reconstruction accuracy of C_p' reconstruction samples is slightly improved based on 10000 samples from each wind direction. Once the training sample size becomes larger, the embedding of $L_{gradient}$ constraint might bring more obvious overfitting, reflected by the higher $\mathrm{RMSE_s}$ and lower R_s^2 criteria.

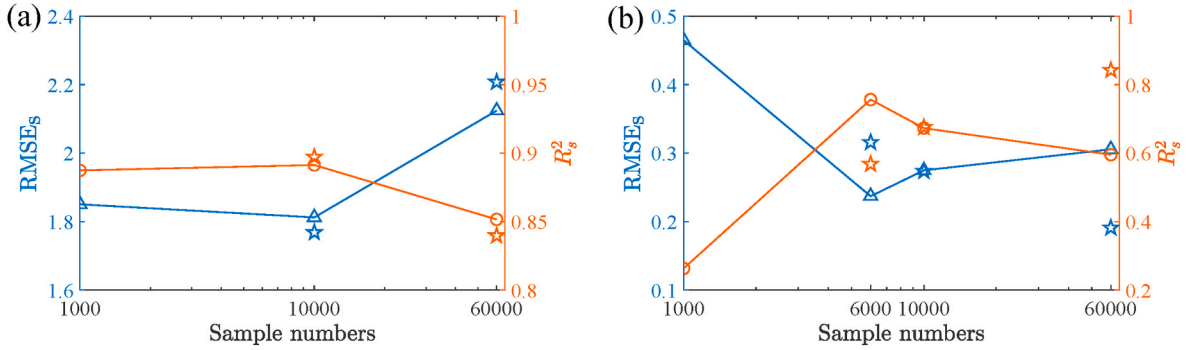

Fig. 21. Dependence of the errors and precisions of the RMS pressure reconstructed by SRCNN without $L_{gradient}$ embedded on the number of training samples, compared with the errors and precisions of $L_{gradient}$ embedded SRCNN for (a) Tile A at $\alpha = +10°$ and (b) Tile B at $\alpha = 180°$.

On Tile B, as the real C_p' values on the tile are distributed more evenly in space than those on Tile A, the predicted accuracies for RMS pressure are easier to experience a sharp climb as the sample size is increased from 1000 to 6000 in Fig. 21(b). Contrast to the Tile A, although the sample size exceeds 10000, the error and accuracy indexes could obtain apparent improvement with the $L_{gradient}$ constraint added, similar to the tendency exhibited in instantaneous C_p distributions from Fig. 21(b). It can be speculated that, compared with the top corner region of the facade (Tile A), there is stronger correlation of the pressure distribution characteristics between different wind direction cases in the middle height of the building near the edge (Tile B), the embedded $L_{gradient}$ constraint is thus easier to enhance the generalization ability of the SRCNN model applied to Tile B.

Appendix B. Selection of the key hyperparameters for SRCNN training

In our study, we determine the batch size and number of residual layers through parameter dependency validation, because they are more

dependent on the classification of problem and the size of dataset than other hyperparameters. The proper hyperparameters are selected considering the balance between the model complexity and the reconstruction accuracy of super-resolution pressure field. Different settings of the two hyperparameters and the comparison of the reconstruction accuracy results are tabulated in Table 4.

In Table 4, take the case of $\alpha = +10^{\circ}$ on Tile A as an example, quantitative comparisons are made for the root mean square error (RMSE) and determination coefficient indexes (R^2) of the reconstructed distribution of instantaneous pressure coefficients. Both indexes are averaged over all moments in the test set according to Eqs. (7) and (8). It can be seen that the batch size has little influence on the reconstruction accuracy of pressure distributions. For the residual block, as layer number increases from 8 to 16, the RMSE error and R^2 accuracy are improved obviously. However, the differences of errors and accuracies remain less 5%, as the layer number increases from 16 to 32. The comparison of the results suggests that the hyperparameter settings, when batch size equal to 16 and layer number of residual block is 16, is sufficient for providing acceptable accuracy for reconstructing the super-resolution pressure fields.

Table 4
Comparison of reconstruction errors and accuracies of instantaneous pressure coefficients by varying the numbers of batch sizes and residual block layers, when $\alpha = +10^{\circ}$ on Tile A.

Key hyperparameters		RMSE	R^2
Batch size	Residual block layers		
8	16	9.9341	0.6013
16	16	9.8252	0.6160
32	16	9.8664	0.6077
16	8	11.5624	0.5378
16	32	9.7591	0.6306

For other hyperparameters of learning rate, kernel size and tolerance are determined according to the settings in Fukami et al. (2020) and Stengel et al. (2020). In their studies, the real details are reproduced well for the super-resolution flow fields by using CNN and GAN. Thus, we apply their corresponding parameters to our SRCNN training.

References

Cao, Y., Tamura, T., Kawai, H., 2019. Investigation of wall pressures and surface flow patterns on a wall-mounted square cylinder using very high-resolution Cartesian mesh. J. Wind Eng. Ind. Aerod. 188, 1–18.

Cao, Y., Wu, H., Chen, Y., Zhou, D., 2022a. An evaluation method of extreme wind pressure on building facades based on machine learning. Dec 5-7. In: The 27th Wind Engineering Symposium. Tokyo, Japan.

Cao, Y., Tamura, T., Zhou, D., Bao, Y., Han, Z., 2022b. Topological description of near-wall flows around a surface-mounted square cylinder at high Reynolds numbers. J. Fluid Mech. 933, A39.

Chen, Y., Wang, Y., Dong, Z., Su, J., Bao, Y., 2021. 2-D regional short-term wind speed forecast based on CNN-LSTM deep learning model. Energ. Convers. Manag. 244 (4), 114451.

Cheng, J., Wang, P., Li, G., Hu, Q., Lu, H., 2018. Recent advances in efficient computation of deep convolutional neural networks. Front. Inform. Tech. El. 19 (1), 64–77.

Cook, N.J., Mayne, J.R., 1980. A refined working approach to the assessment of wind loads for equivalent static design. J. Wind Eng. Ind. Aerod. 6 (1–2), 125–137.

Darren, P., Rasim, L., Jon, P., Jason, D., 2018. Landsat super-resolution enhancement using convolution neural networks and sentinel-2 for training. Rem. Sens. 10 (3), 394.

Fukami, K., Fukagata, K., Taira, K., 2020. Machine learning based spatio-temporal super resolution reconstruction of turbulent flows. J. Fluid Mech. 909, A9.

He, K., Zhang, X., Ren, S., Sun, J., 2016. Residual learning for image recognition. In: Proceedings of IEEE Conference on Computer Vision and Pattern Recognition, pp. 770–778. Las Vegas, USA.

Holmes, J.D., 1997. Equivalent time averaging in wind engineering. J. Wind Eng. Ind. Aerod. 72, 411–419.

Hu, G., Liu, L., Tao, D., Song, J., Tse, K.T., Kwok, K.C.S., 2020. Deep learning-based investigation of wind pressures on tall building under interference effects. J. Wind Eng. Ind. Aerod. 201, 104138.

Huang, P., Peng, X., Gu, M., 2014. Aerodynamic devices to mitigate rooftop suctions on a gable roof building. J. Wind Eng. Ind. Aerod. 135, 90–104.

Huang, D., He, S., He, X., Zhu, X., 2017. Prediction of wind loads on high-rise building using a BP neural network combined with POD. J. Wind Eng. Ind. Aerod. 170, 1–17.

Hui, Y., Yoshida, A., Tamura, Y., 2013. Interference effects between two rectangularsection high-rise buildings on local peak pressure coefficients. J. Fluid Struct. 37, 120–133.

Jin, X., Cheng, P., Chen, W., Li, H., 2018. Prediction model of velocity field around circular cylinder over various Reynolds numbers by fusion convolutional neural networks based on pressure on the cylinder. Phys. Fluids 30, 047105.

Keerthana, M., Harikrishna, P., 2017. Wind tunnel investigations on aerodynamics of a 2: 1 rectangular section for various angles of wind incidence. Wind Struct. 25 (3), 301–328.

Kim, Y.C., Yoshida, A., Tamura, Y., 2012. Characteristics of surface wind pressures on low-rise building located among large group of surrounding buildings. Eng. Struct. 35, 18–28.

Kopp, G., Morrison, M., Gavanski, E., Henderson, D., Hong, H., 2010. "Three Little Pigs" project: hurricane risk mitigation by integrated wind tunnel and full-scale laboratory tests. Nat. Hazards Rev. 11 (4), 151–161.

Lamberti, G., Amerio, L., Pomaranzi, G., Zasso, A., Gorlé, C., 2020. Comparison of high resolution pressure measurements on a high-rise building in a closed and opensection wind tunnel. J. Wind Eng. Ind. Aerod. 204, 104247.

Lawson, T., 1976. The design of cladding. Build. Environ. 11 (1), 37–38.

Li, S., Laima, S., Li, H., 2018. Data-driven modeling of vortex-induced vibration of a long-span suspension bridge using decision tree learning and support vector regression. J. Wind Eng. Ind. Aerod. 172, 196–211.

Li, D., Liu, B., Zhou, X., Wang, Z., 2021. Size effects of area extreme pressure for large-scale cladding. Structures 29, 408–415.

Lin, P., Hu, G., Li, C., Li, L., Xiao, Y., Tse, K.T., Kwok, K.C.S., 2021. Machine learning-based prediction of crosswind vibrations of rectangular cylinders. J. Wind Eng. Ind. Aerod. 211, 104549.

Lin, P., Ding, F., Hu, G., Li, C., Xiao, Y., Tse, K.T., Kwok, K.C.S., 2022. Machine learning-enabled estimation of crosswind load effect on tall buildings. J. Wind Eng. Ind. Aerod. 220, 104860.

Newberry, C.W., Eaton, K.J., Mayne, J., 1973. Wind Loading on Tall Buildings: Further Results from Royex House, Building Research Establishment. Building Research Station.

Okuda, Y., Taniike, Y., 1993. Conical vortices over side face of a three-dimensional square prism. J. Wind Eng. Ind. Aerod. 50, 163–172.

Pomaranzi, G., Amerio, L., Zasso, A., 2020. Wind tunnel test data on high-rise building, Zenodo, Politecnico di Milano, vol. 1. https://zenodo.org/record/3948348.

Pomaranzi, G., Amerio, L., Schito, P., Lamberti, G., Gorlé, C., Zasso, A., 2022. Wind tunnel pressure data analysis for peak cladding load estimation on a high-rise building. J. Wind Eng. Ind. Aerod. 220, 104855.

Rodrigues, E.R., Oliveira, I., Cunha, R.L.F., Netto, M.A.S., 2018. Deep Downscale: a Deep Learning Strategy for High-Resolution Weather Forecast. IEEE International Conference on E-science, Amsterdam, Netherlands, pp. 415–422.

Sang, J., Pan, X., Lin, T., Liang, W., Liu, G.R., 2021. A data-driven artificial neural network model for predicting wind load of buildings using GSM-CFD solver. Eur. J. Mech. B Fluid 87, 24–36.

Stengel, K., Glaws, A., Hettinger, D., King, R., 2020. Adversarial super-resolution of climatological wind and solar data. P. Natl. Acad. Sci. 117 (29), 16805–16815.

Surry, D., Djakovich, D., 1995. Fluctuating pressures on models of tall buildings. J. Wind Eng. Ind. Aerod. 58 (1–2), 81–112.

Uematsu, Y., Tsuruishi, R., 2008. Wind load evaluation system for the design of roof cladding of spherical domes. J. Wind Eng. Ind. Aerod. 96 (10–11), 2054–2066.

Wang, H., Wu, W., Su, Y., Duan, Y., Wang, P., 2019. Image Super-resolution Using a Improved Generative Adversarial Network. Proceedings of IEEE 9th International Conference on Electronics Information and Emergency Communication, Beijing, China, pp. 312–315.

Yousif, M., Yu, L., Lim, H., 2021. High-fidelity reconstruction of turbulent flow from spatially limited data using enhanced super-resolution generative adversarial network. Phys. Fluids 33 (12), 125119.
Yousif, M., Yu, L., Lim, H., 2022. Super-resolution reconstruction of turbulent flow fields at various Reynolds numbers based on generative adversarial networks. Phys. Fluids 34, 015130.
Zhang, J., Li, Q., 2018. Field measurements of wind pressures on a 600m high skyscraper during a landfall typhoon and comparison with wind tunnel test. J. Wind Eng. Ind. Aerod. 175, 391–407.